

REPORT DOCUMENTATION PAGE

Form Approved
OMB No. 0704-0188

The public reporting burden for this collection of information is estimated to average 1 hour per response, including the time for reviewing instructions, searching existing data sources, gathering and maintaining the data needed, and completing and reviewing the collection of information. Send comments regarding this burden estimate or any other aspect of this collection of information, including suggestions for reducing the burden, to the Department of Defense, Executive Service Directorate (0704-0188). Respondents should be aware that notwithstanding any other provision of law, no person shall be subject to any penalty for failing to comply with a collection of information if it does not display a currently valid OMB control number.

PLEASE DO NOT RETURN YOUR FORM TO THE ABOVE ORGANIZATION.

1. REPORT DATE (DD-MM-YYYY) 30-01-2012		2. REPORT TYPE Final		3. DATES COVERED (From - To) Aug 31 2008 - Sep 30 2011	
4. TITLE AND SUBTITLE AERO-EFFECTED FLIGHT CONTROL USING DISTRIBUTED ACTIVE BLEED				5a. CONTRACT NUMBER	
				5b. GRANT NUMBER FA9550-08-1-0398	
				5c. PROGRAM ELEMENT NUMBER	
6. AUTHOR(S) Ari Glezer and Anthony Leonard				5d. PROJECT NUMBER	
				5e. TASK NUMBER	
				5f. WORK UNIT NUMBER	
7. PERFORMING ORGANIZATION NAME(S) AND ADDRESS(ES) Woodruff School of Mechanical Engineering Georgia Institute of Technology Atlanta, GA 30332-0405				8. PERFORMING ORGANIZATION REPORT NUMBER N/A	
9. SPONSORING/MONITORING AGENCY NAME(S) AND ADDRESS(ES) USAF AFMC AFOSR/RSA 875 N. Randolph St. Suite 325 Arlington, VA 22203				10. SPONSOR/MONITOR'S ACRONYM(S)	
				11. SPONSOR/MONITOR'S REPORT NUMBER(S) AFRL-OSR-VA-TR-2012-0276	
12. DISTRIBUTION/AVAILABILITY STATEMENT Unlimited					
13. SUPPLEMENTARY NOTES					
14. ABSTRACT Aero-effected flight control using distributed active bleed driven by pressure differences on lifting surfaces and regulated by low-power louver actuators was investigated experimentally and theoretically. The flow mechanisms of the interaction between unsteady bleed and the cross flows were investigated on a 2-D static and dynamically pitching Clark-Y model integrated with piezoelectric louvers. The effects of leading and trailing edge bleed on the aerodynamic forces and the flow field were measured using load cells and PIV. Trailing edge bleed at low AoA effects nearly-linear variation of the pitching moment ($\pm 12\%$) with minimal drag penalty. Leading edge bleed at high AoA leads to large variations in lift and pitching moment, and extends the stall margin enabling up to 50% variation in the baseline lift without external control surfaces. Numerical simulations using immersed boundary and penalty methods, showed that the bleed near the trailing edge induced changes in circulation to maintain the Kutta condition. This change in circulation accounts for 5/7 of the total change in lift with center-of-pressure at $c/4$, in accordance with classical theory. A vortex-based reduced order model was developed to predict aerodynamic forces on an arbitrarily pitching and plunging airfoil with unsteady bleed. Bleed actuation was also investigated on a pitching airfoil over a wide range of AoA. At high reduced frequencies ($k > 0.1$), the bleed alters the dynamics of vorticity production and advection and interacts with the dynamic stall vortex to increase the stability of the pitch motion and minimize negative damping with low lift penalty.					
15. SUBJECT TERMS aerodynamic bleed, active control, louvers, lift and pitch control, vortex based reduced order model					
16. SECURITY CLASSIFICATION OF:			17. LIMITATION OF ABSTRACT	18. NUMBER OF PAGES	19a. NAME OF RESPONSIBLE PERSON
a. REPORT	b. ABSTRACT	c. THIS PAGE			19b. TELEPHONE NUMBER (include area code)

Aero-Effectuated Flight Control Using Distributed Active Bleed

AFOSR Grant FA9550-08-1-0398

Final technical Report

Ari Glezer¹ and Anthony Leonard²

¹Woodruff School of Mechanical Engineering, Georgia Institute of Technology

²Graduate Aeronautical Laboratories, California Institute of Technology

Abstract

A novel, scalable approach to aero-effectuated flight control of lifting surfaces using distributed active bleed was investigated experimentally and theoretically. Aerodynamic control is achieved by large-area surface bleed of air that is driven by the pressure differences in flight and is regulated by low-power surface-integrated louver actuators. The joint numerical-experimental investigation focused on the flow mechanisms of the interaction between the bleed and the cross flow and aerodynamic effects of unsteady bleed on a 2-D wing model. Particular emphasis was placed on the generation and regulation of vorticity concentrations that alter the wing's apparent aerodynamic shape and thereby its aerodynamic performance over a range of (static) angles of attack, and under time-periodic pitch oscillations. Wind tunnel investigations of the mechanisms of the time-dependent interactions between the bleed and cross flows used a 2-D Clark-Y model integrated with addressable arrays of piezoelectric louvers for regulating leading and trailing edge bleed. The resulting time-dependent forces and moment were measured over a wide range of angles of attack from pre- to post-stall using load cells, and the induced changes in surface vorticity concentrations were measured using PIV. Trailing edge bleed at low angles of attack effects nearly-linear variation of the pitching moment ($\pm 12\%$) with minimal drag penalty. Leading edge bleed at high angles of attack leads to large variations in lift and pitching moment, and it can also be used to extend the stall margin using time-periodic louver actuation. At high angles of attack, leading-edge bleed actuation enables up to 50% variation in lift relative to the baseline without the use of external control surfaces. The laboratory experiments were accompanied by computational and theoretical investigations. The numerical simulations were performed assuming two-dimensional flow at low to moderate Reynolds numbers. Navier-Stokes solvers using the immersed boundary method and the penalty method, suitable for the complex geometries involved, were employed. It was shown that the global effect of bleed near the trailing edge is due to a change in airfoil circulation required to maintain the Kutta condition at the trailing edge in the presence of bleed. This latter change in circulation also corresponds to reduction of lift due to bleed and accounts for five sevenths of the total change in lift coefficient with a center-of-pressure at quarter chord, in accordance with classical theory. As a part of the theoretical effort, a vortex-based reduced order model was developed for trailing-edge bleed. The model, which is based on interplay between experiments and theory, predicts unsteady airfoil lift and moment for an arbitrarily pitching and plunging airfoil with unsteady bleed. Bleed actuation is also investigated on a pitching airfoil over a wide range of angles of attack. At high reduced frequencies ($k > 0.1$), the bleed significantly alters the dynamics of vorticity production and advection and interacts with the dynamic stall vortex to increase the stability of the pitch motion, minimizing negative damping with relatively low penalty in lift.

I. OVERVIEW

In contrast to conventional flow control technologies in which actuation relies on momentum transfer to the cross flow either mechanically (e.g. flaps, Liu, Tsao, Tai, and Ho, 1994), fluidically (control jets, Glezer and Amitay, 2002), by induced body forces (plasma, Corke, 2005 or electromagnetic actuation, Fan and Brown, 1997), or by heating (Liepmann and Nosenchuck, 1982), *the primary mechanical energy required to effect flow control by aero-bleed actuation is derived from the motion of the vehicle.* Actuation is applied by regulation of the bleed flow using low-power distributed surface valves which may be thought of as analogous to the role of a transistor's base current that regulates the much higher current between the emitter and the collector. However, while in common with zero net mass flux (synthetic jet) actuation, active bleed utilizes fluid from the embedding flow, and its operating bandwidth is clearly bounded by the characteristics of the fluidic circuit including the magnitude of the available pressure drop, the advection length, flow path resistance and capacitance, etc.

The use of passive porosity for aerodynamic flow control by exploiting inherent pressure differences over surfaces of moving bodies is not new and has been explored in a number of earlier investigations. In a typical application fluid is bled from high- to low-pressure domains through porous surface segments through an internal passage or a plenum. The ensuing interaction of the ejection or suction with the cross flow can result in a local modification of the pressure distribution (and pressure gradients), lead to alteration of the flow over the surface, and in some cases result in global changes in aerodynamic forces. Several examples include reduction of the drag of bluff bodies by base bleed (Tanner, 1975), laminar flow control (Carpenter and Porter, 2001), tip vortex control (Han and Leishman, 2004), aerodynamic maneuvering forces (Hunter, Viken, Wood, and Bauer, 2001), mitigation of flow separation (Lopera, Ng, and Patel, 2004), and reduction of shock-induced separation on transonic airfoils (Savu and Trifu, 1984). It is noteworthy that studies of multiple slots that act as conduits for bleed flow between the pressure and suction side of various airfoils were investigated as early as the 1920s (Lachmann, 1924, and Weick and Shortal, 1932).

Extensive investigations of passive porosity for alteration of the aerodynamic forces on aircraft have been undertaken by Bauer and his co-workers (dubbed PassPorT) where the characteristic dimensions of the holes in the porous surfaces were selected to be small compared to the boundary-layer thickness and smaller than or equal to the skin thickness with relatively low flow rates. In their work on projectiles forebodies (Bauer and Hemsch, 1993, Frink, et al., 2003), passive porosity was used to reduce the side forces or yawing moments on porous forebodies over a broad range of angles of attack and for effecting localized reduction in lift to provide roll and yaw control. The numerical work of Tinetti et al. (2001) demonstrated that passive porosity can be used to reduce the unsteady lift force developed on an airfoil by a moving wake that is similar to the unsteady forces associated with rotor-stator interactions in turbomachinery. The authors showed that porosity over $0.1c$ downstream of the leading edge on the suction side coupled with porosity on different segments of the pressure side results in attached flow and can reduce the magnitude of the unsteady lift by as much as 18% without significant performance losses. Finally, Hunter et al. (2001) considered passive porosity control for a generic tailless fighter aircraft and their numerical simulations showed that at low-speed and high angles of attack passive porosity can provide maneuver control that is similar to that of conventional control surfaces.

Actively controlled porosity effects using switched or reconfigurable porous surfaces were also investigated. Patel, DiCocco, Prince, and Ng (2003) showed that different patterns of porous segments on munitions wings could lead to variations of the aerodynamic forces. This work was connected to the development of microfabricated valve arrays by Lopera, Ng, and Patel (2004). Another attempt to control bleed by using microfabricated valves (Ho, Nassef, Pornsinsirak, Tai, and Ho, 2003) was limited by high pressure drops across these miniature valves which severely limited the flow through the porous surfaces. It is noteworthy that Ho et al. (2003) used a self-actuated check valve that was integrated into a small, thin-membrane flapping wing and achieved considerable improvement in its aerodynamic performance.

The present investigations focus on the aerodynamic effects of controlled, large-area distributed active bleed that is driven by pressure differences across a Clark-Y airfoil model. Forces and moments are altered and regulated by fluidic modification of the apparent aerodynamic shape using surface-integrated piezoelectrically-driven louvers. Static and dynamic actuation modes over a range of angles of attack are used to effect interaction between bleed and cross flows with significant effects on the aerodynamic forces and moments. The experiments were accompanied by computational and theoretical investigations to develop a fundamental understanding of the aerodynamics of unsteady bleed and to determine its potential for active control of aircraft.

II. EXPERIMENTAL APPARATUS

II.1. Wind Tunnel Facility and Diagnostics

The present investigation is conducted in a low-speed closed-return atmospheric wind tunnel having a rectangular test section measuring 25 x 47 x 132 cm with optical access from all sides (test section speed ranges from 3 to 35 m/sec). The flow is driven by an 18" centrifugal blower coupled to a 15 HP electric motor connected to a computer-controlled speed controller. The tunnel has a 9.25:1 contraction and an inline chilled water heat exchanger to maintain a constant temperature in the test section. The experiments reported here were conducted at $Re = 190,000$ ($U_o = 15\text{m/s}$, $T_{\text{conv}} = 13.3\text{ms}$).

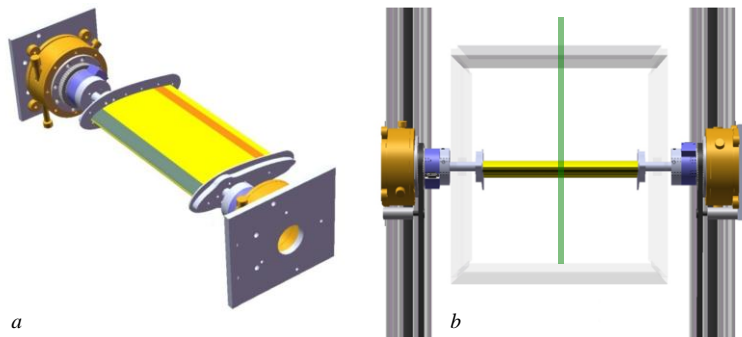


Figure II.1. The Clark-Y airfoil model suspended between the load cells, showing (a) a perspective view with the load cell mounts (spanwise bleed configurations are marked in blue and red), and (b) a head-on view of the airfoil in the wind tunnel including the PIV measurement plane.

The airfoil model is mechanically isolated from the test section and is mounted on an external frame that surrounds the test section. It is suspended between two external six-axis strain-gage load cells, (0.002N/mV resolution, maximum frequency response 500 Hz), by compliant couplings through the quarter chord that isolate the lift and drag forces and the pitching moment (Figure II.1a). The output of each of the load cell amplifiers (up to $\pm 10\text{V}$) is digitized using a 16-bit National Instruments board. Each load cell is mounted on a rotational servo motor (the dynamic pitch system is described in §II.2), and the two motors are used in concert to control the

airfoil's angle of attack α during static and closed-loop dynamic pitch tests. As α varies, the loads are computed and transformed in real time to aerodynamic forces and the pitching moment.

In addition to force measurements, static pressure distributions are obtained using 32 static ports around the circumference of the airfoil at mid-span. These connect to an external high-speed scanner and are transferred to the laboratory computer over ethernet. The velocity field is measured in cross stream planes above the airfoil and in the near wake (Figure II.1b) using high-resolution PIV (1600 x 1200 pixel, 14-bit CCD camera).

II.2. Pitching Traverse

A traverse mechanism for dynamic pitch of the airfoil model was constructed specifically for the present experiments (Figure II.2). As noted in §II.1, the traverse and the model are isolated from the tunnel's test section. The traverse frame surrounds the test section is constructed from 1" and 3/4" thick structural steel plates that are bolted together, and is attached to an optical table by four vibration isolators. This construction yields a simple, stiff, high-mass frame that is isolated from blower vibrations transmitted through the wind tunnel's frame.

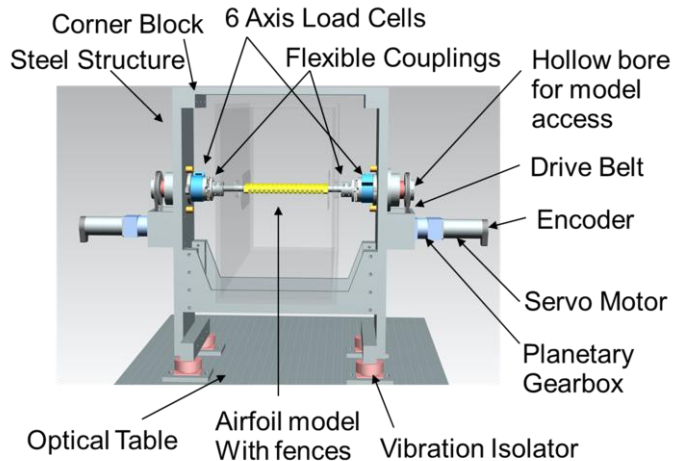


Figure II.2. The pitching traverse.

The model is driven at both spanwise edges by identical mechanisms shown in Figure II.3. Each mechanism is based on a hollow axle riding in a pair of deep groove ball bearings. The pair of axle bearings are preloaded against one another to eliminate axial play without introducing binding. Each load cell is bolted to the inner surface face of the axle, and flexible shaft couplings are bolted to the outer face of the load cells. The model is then suspended between the flexible shaft couplings by removable cap clamps cut into the inner side of the flexible shaft couplings. The hollow axle is turned by a timing belt drive (2:1 ratio). The offset allowed by the timing belt final drive allows passage of wiring and pressure port tubing to the interior of the model. The primary side of the timing belt is driven by a 3-phase brushless DC servo motor mated to a 10:1 planetary box. A 2,500 quadrature cycle per revolution (10,000 counts/revolution) differential output encoder is mounted on the outboard of the motor shaft for position feedback. The flexible couplings allow for axial and angular

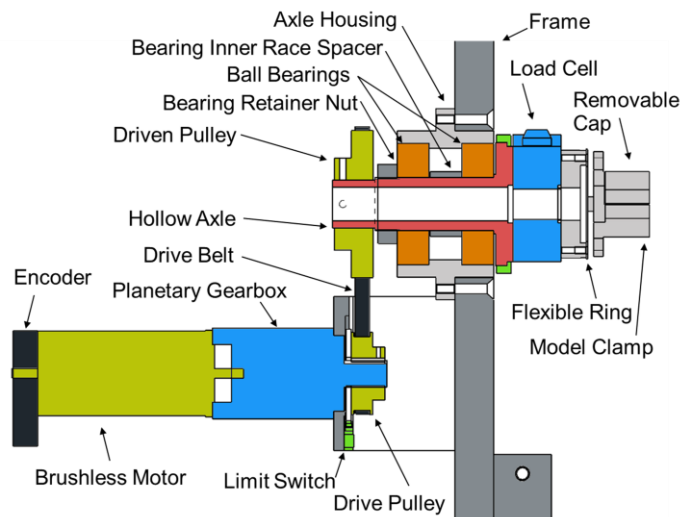


Figure II.3. The servomotor assembly.

deflections of each end of the model, but are stiff in torsion. This compliance compensates for any structural imperfection in the traverse (parallel or axial misalignment between the two sides, or even temperature driven strain). The primary beam bending resonant frequency is designed to be above the range of pitching frequencies that are of interest in the present implementation.

The pitch motors are driven by servo amplifiers ($\pm 10V$ command input) configured to current (torque) mode and are powered by a 30 VDC unregulated power supply. A National Instruments 4-axis motion controller board is used in concert with an existing LabView-based data acquisition computer. The control board is configured to run independent position control, manually tuned PID loops on both sides of the traverse. To perform a given motion, the same position trajectory is supplied to both axes. Analog angular position is available for triggering and sampling for synchronization with other data signals.

The DAQ software is split into three parts. The first part primarily controls the controller board and is used to start and stop the model motion, feed position coordinates to the motion buffer, and generate a TTL trigger pulse synchronized to the model's motion (a periodic trigger pulse was generated for static experiments). The second part of the software is responsible for generating AO synchronization signals, AO actuator commands, and performing analog data acquisition over multiple pitch cycles on rising edges of the trigger pulse. The third (collective) part of the software includes interactive programs that control and synchronize the experiment by executing load cell acquisition, generating and outputting arbitrary bleed actuation waveforms, analyzing frequency-domain aspects of sampled signals in real time, and recording data.

II.3. The Airfoil

The Clark-Y airfoil model was selected for both its stable lift and stall characteristics and its relatively flat bottom surface from $0.3 < x/c < 1$ (which aids in the installation of piezoelectric louvers, but is not crucial to enable bleed technology). The airfoil model is fabricated using stereolithography (SLA), and the resin chosen maximizes the average ratio of tensile modulus to weight (18.33 MPa/g) to ensure the model is both stiff and lightweight. The geometry of the model is designed to enable several bleed configurations through spanwise rows of surface grids through the pressure and suction surfaces. The model has a 20 cm chord and spans almost the entire width of the test section (20.3 cm) with maximum thickness of $0.12c$ at $0.36c$. Plexiglass compression endplates reduce three dimensional flow effects due to the airfoil's finite span and are connected with shafts to the load cells outside the tunnel. The interior of the airfoil is hollow except for a reinforcing truss along the midspan and silicone-shielded wires, which exit the airfoil and test section through the shafts. The model could be stiffened by adding internal

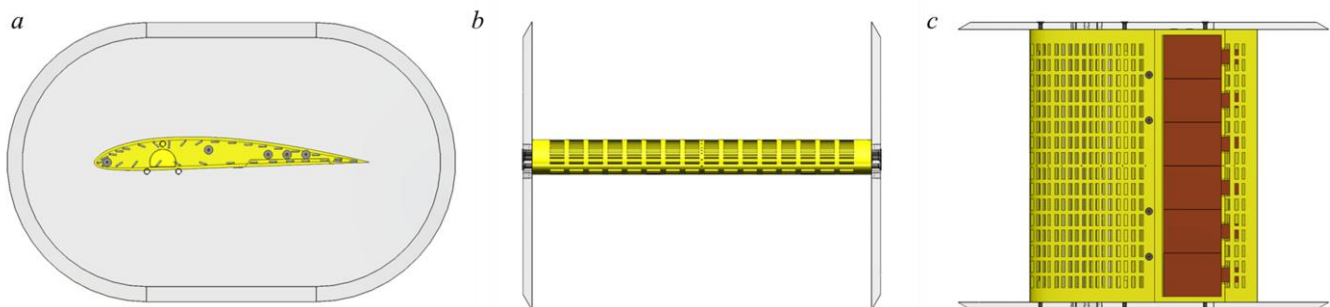


Figure II.4. (a) Side-view of the airfoil depicting outlets for static pressure taps, (b) head-on view, and (c) bottom-view showing the spanwise array of piezoelectric louvers.

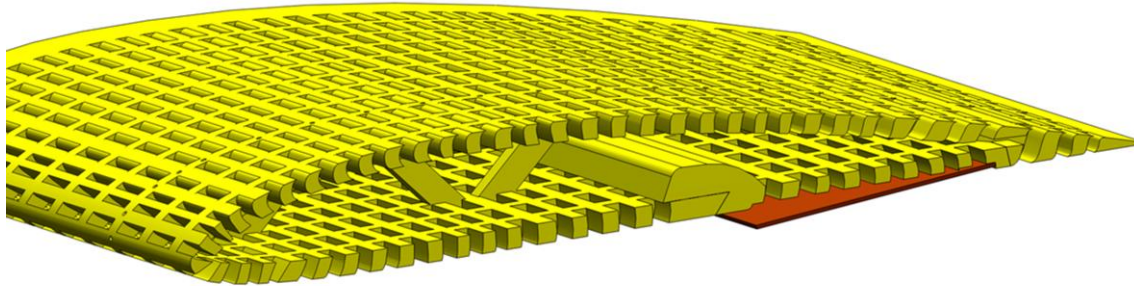


Figure II.5. Cutaway view of the airfoil showing the contoured bleed passages in the upper and lower surfaces. Louvers on the pressure side open to drive flow into the interior plenum.

thickened spanwise structures from the pressure and suction sides that interleave to form a quasi-spar, but would add some resistance to the bleed. The large-area, low-resistance surface grid (with a total of 826 bleed ports) is open to the inner volume of the model, and bleed flow exits through orifices in the grid. Paths to pressure taps are embedded in the SLA skin and are routed to the endplate (Figure II.4a), where steel and flexible tubing transmit the pressure force out of the test section to the scanner. The head-on view in Figure II.4b shows the bleed grid density and pressure taps along the mid-chord. This design takes advantage of the flexibility of SLA prototyping by providing a higher grid density near the leading edge, where the variation in airfoil surface curvature is the highest, and enables precise control over the location of bleed outlet flow and therefore of the interaction with the cross flow. By sealing portions of the grid with thin adhesive tape (thickness of 0.0015in), virtually unlimited combinations of bleed configurations are accessible for testing, including bleed from ports on the leading edge to ports within $0.04c$ of the trailing edge. Figure II.4c shows the piezoelectric louver actuators (brown) in the airfoil surface. These actuators are individually addressable or may be driven simultaneously.

Figure II.5 shows a section view of the airfoil in which the louvers, structural members, and bleed passages are visible. Upon actuation the louvers displace from the surface to uncover bleed inlets. Uncovering additional openings in the bleed grid (where the local static pressure is lower) allows flow to communicate between desired locations on the airfoil surface. Each bleed passage is contoured so that the exit flow is nominally tangential to the airfoil surface. Note that the structural component to which the louvers are attached in Figure II.5 is modular and may be replaced or modified. Figures II.6a and b show two particularly effective bleed configurations through the leading and trailing edges, which will be discussed in detail later.

II.4. Louver Actuators

In the present experiments, the louver actuators are arranged in a spanwise array on the pressure side upstream of the trailing edge where each planar actuator (measuring 51 x 38 mm) is recessed so that it is flush with the surface when it is inactive, is cantilevered along its downstream end, and regulates the flow through the bleed

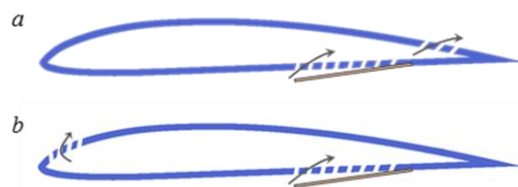


Figure II.6. Bleed through the airfoil between (a) the pressure and suction surfaces near the trailing edge (louver actuation uncovers the inlet orifices on the pressure side) and (b) from the pressure surface near the trailing edge to the suction surface near the leading edge.

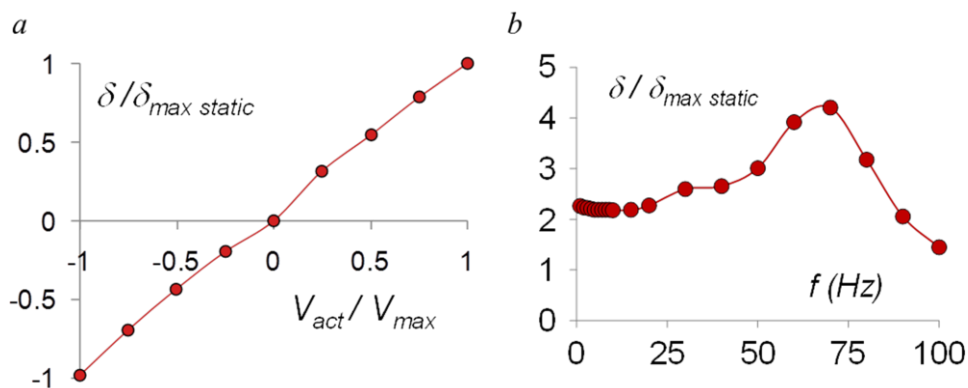


Figure II.7. (a) Variation of normalized lower tip displacement with normalized actuation voltage, and (b) variation of lower tip displacement with actuation frequency.

inlets by lifting off the surface (Figure II.5). In the spanwise direction, the louvers are spaced less than 0.010in apart to avoid interference during actuation, and the surface grid underneath each space is sealed to prevent inflow leakage. The piezoelectric planar bimorph actuators are capable of two-way deflection, have a reasonably broad response from DC up to 150 Hz, and each is individually addressable from the laboratory computer (via a D/A interface) using an arbitrary waveform, as noted in §II.2.

The static and dynamic performance of the actuators was quantified using an optical rangefinder to monitor their motion. The static displacement of each louver normalized by its maximum static displacement δ_{max} (Figure II.7a) varies linearly with the applied voltage and thus can consistently regulate the bleed flow. Louver displacements larger than 8 mm (0.04c) can be realized. Time-periodic louver motion is applied with an arbitrary DC offset, and the frequency response of the louvers to a sinusoidal waveform is shown in Figure II.7b, which indicates a resonance frequency peak near 70Hz.

III. AERODYNAMIC PERFORMANCE OF THE BASELINE AIRFOIL

The performance of a baseline “sealed” airfoil which has no open bleed ports but is otherwise identical to the bleed model was established. The static variations with angle of attack of C_L , C_D , and C_M at $Re = 190,000$ are shown in Figure III.1. The airfoil exhibits stable lift characteristics, as C_L increases linearly with incidence angle up to $\alpha = 14^\circ$ at a rate of $dC_L/d\alpha = 1.6\pi\alpha$, (compared to $dC_L/d\alpha = 2\pi\alpha$ for a 2-D flat plate airfoil). The lift saturates at $C_L \approx 1.5$ within the range $14^\circ < \alpha < 18^\circ$. At the onset of static stall, C_L is reduced by nearly 25% and does not

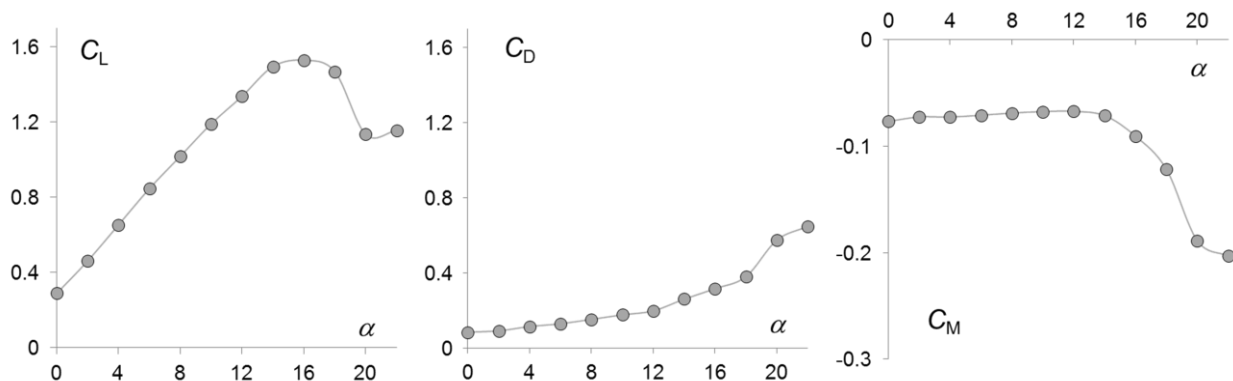


Figure III.1. Variations with angle of attack in C_L , C_D , and C_M for the baseline airfoil.

recover pre-stall levels of lift until angles higher than 30° (not shown). Drag levels are low for all angles and increase monotonically, reaching a pre-stall maximum of 0.38 at $\alpha = 18^\circ$ (26% of C_L).

During stall, flow separation increases form drag and momentarily increases $dC_D/d\alpha$ between $18^\circ < \alpha < 20^\circ$, but the pre-stall slope resumes for $\alpha > 20^\circ$. The airfoil model is pitched about the quarterchord, and in agreement with theory the pitching moment remains relatively constant throughout low to moderate angles, indicating that the aerodynamic center remains at a fixed location in this range. Here, $C_M \approx -0.07$ until 14° , where it begins to decrease as stall progresses. Negative values of C_M correspond to nose-down pitch, showing that the pitching moment

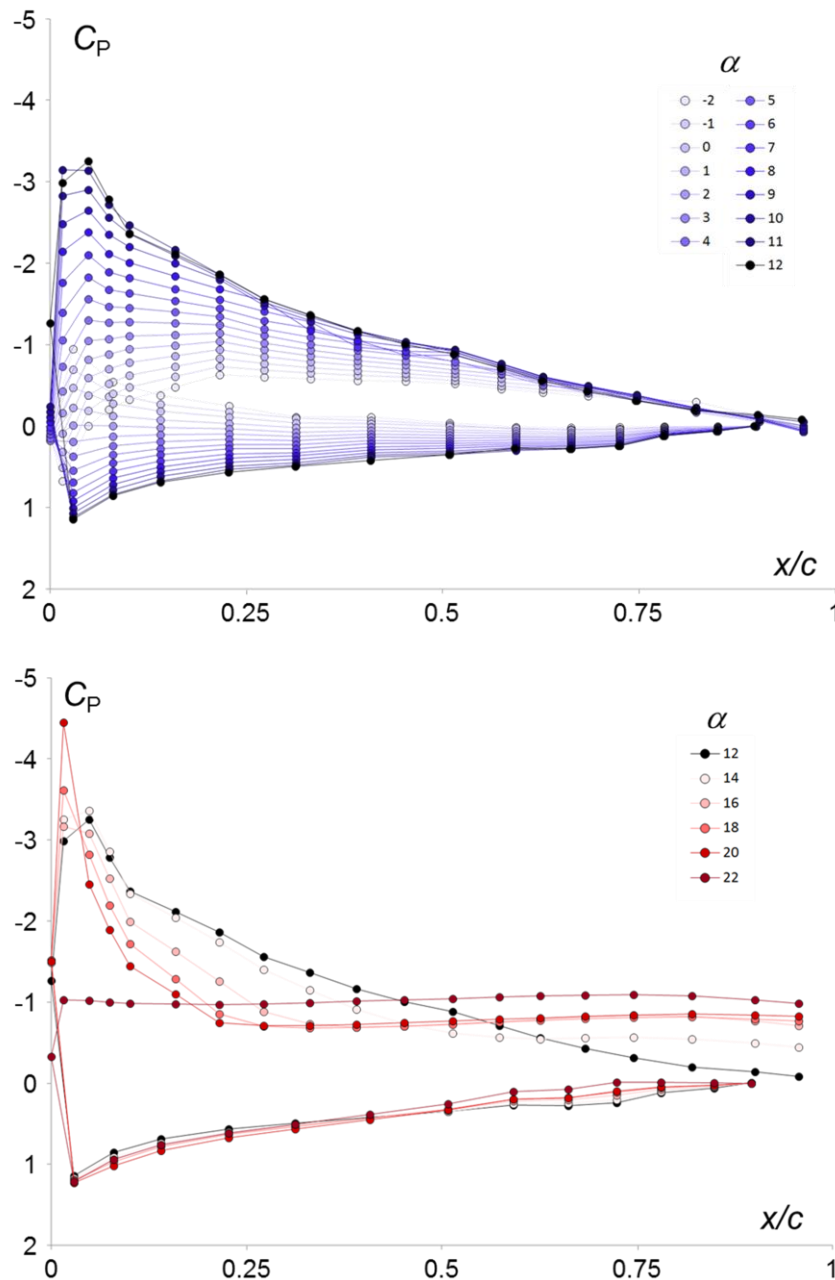


Figure III.2. Static pressure distributions around the baseline airfoil: $-2^\circ < \alpha < 12^\circ$ (top) and $12^\circ < \alpha < 22^\circ$ (bottom).

counteracts the pitch-up tendency due to strong suction near the leading edge under stable flow conditions. Through stall, the location of the net pressure force responsible for generating the pitching moment shifts aft of $c/4$, and $dC_M/d\alpha < 0$, indicating longitudinal static stability.

Figure III.2 shows a compilation of time-averaged distributions of static pressure data over the chord of the baseline airfoil that indicate the variation of the static pressure distribution when the flow is fully attached ($-2^\circ < \alpha < 12^\circ$, top), and during the onset and upstream progression of separation towards the leading edge ($12^\circ < \alpha < 22^\circ$, bottom). At low angles ($\alpha < 1^\circ$) the leading-edge suction peak is reversed within the range $0 < x/c < 0.025$, indicating that the stagnation point rests on the upper surface of the airfoil. As α increases, suction builds within $0 < x/c < 0.5$ while the pressure increases on the bottom surface. Note that structural limitations of the model's thickness prevent the placement of pressure tap on the pressure side near the trailing edge ($0.9 < x/c < 1$). The first signs of flow separation are evident at $\alpha = 14^\circ$, where suction pressure on the upper surface is nearly invariant ($C_p = -0.55$) for $0.63 < x/c < 1$ (note that this also corresponds to turning point for $C_M(\alpha)$ in Figure III.1). Therefore the separated domain near the trailing edge is subjected to negative pressure that is responsible for pitching the airfoil nose-down. The separation point advances upstream to $x/c = 0.33$, 0.27 , and 0.21 at $\alpha = 16^\circ$, 18° , and 20° , respectively. Over these angles the domain of the nearly invariant pressure that is associated with separated flow increases and the width of the suction peak near the leading edge diminishes (corresponding to an overall decrease in lift). Note that the stagnation point near the leading edge on the lower surface of the airfoil remains relatively invariant through these angles. By $\alpha = 22^\circ$, the suction peak is eliminated on the top surface of the airfoil and the static pressure, $C_p = -1.0$, is unchanged along the entire airfoil chord.

The effect of the operating louvers on the aerodynamic characteristics of the airfoil in the absence of bleed (i.e. when the airfoil is sealed) is assessed from load cell measurements. Figure III.3 shows the changes in lift, drag, and pitching moment relative to the baseline with fractional louver opening A over a range of angles of attack. These data show that the extension of the louvers into the cross flow on the pressure side leads to minimal interference. The maximum changes in drag, lift, and pitching moment induced by the louver actuation are as 1.6%, 2.6%, and 3.3%, respectively.

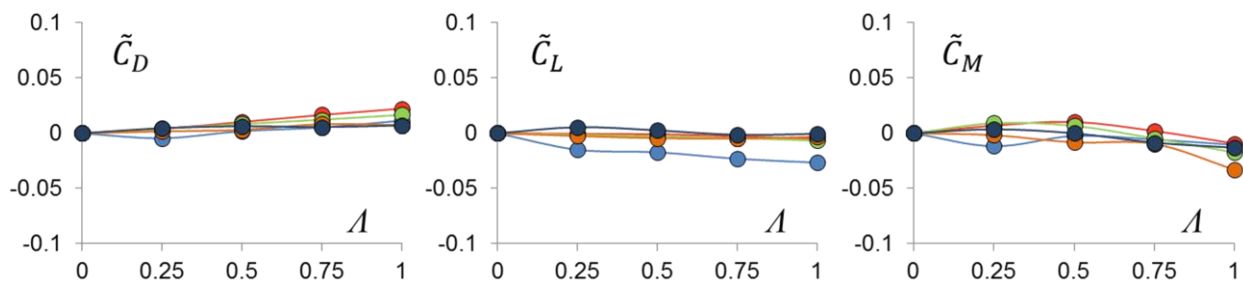


Figure III.3. Effects of static louver actuation on aerodynamic forces in the absence of bleed:

$\alpha = 4^\circ$ (●), 8° (●), 12° (●), 16° (●), and 20° (●).

IV. TRAILING EDGE BLEED ACTUATION, STATIC AIRFOIL

IV.1. Experimental and Computational Results

One of the main objectives of the present work is to develop a fundamental understanding of the aerodynamics of active bleed. The laboratory experiments described in this report are

augmented by computational experiments using Navier-Stokes solvers designed to handle the complex geometries of the distributed bleed. The first effort employs the immersed boundary method in which the geometry is gridded with a regular Cartesian mesh and forces distributed near the airfoil boundaries are used to enforce the no-slip condition while satisfying the incompressibility constraint. Another series of simulations is made using the penalty method, similar in approach to the immersed boundary method except that the no-slip condition is applied in a different manner.

A reduced-order model for a pitching, plunging airfoil with arbitrary unsteady, trailing-edge bleed is also developed. The flows of interest for this project are characterized by regions of concentrated vorticity in the boundary layer and in the wake of the airfoil with distributed sources and sinks on the surface of the airfoil. Thus, the model is based on the kinematics and dynamics of vorticity in the flow with suitable simplifications and approximations. The resultant model is robust and accurate in predicting time-dependent lift and moment and provides further insight into the flow physics of the flow-induced bleed.

Crucial to the development of the model is guidance by the results of laboratory and computational experiments, in which bleed actuation is used near the trailing edge (cf. Figure II.6a) to modify the aerodynamic characteristics of the airfoil when the baseline flow is fully attached at low angles of attack. Bleed is effected within the domain $0.76 < x/c < 0.85$ on the suction side of the airfoil using an array of integrated louvers on the pressure side. The magnitude of the bleed is controlled by static deflection of the louvers, and the resulting changes in the aerodynamic forces and in the pitching moment are shown in Figure IV.1 for $\alpha = 4^\circ, 8^\circ$, and 12° ($Re = 190,000$). These data show the variation with the fractional louver opening A of the (normalized) increments in aerodynamic loads relative to the baseline and to $A = 0.5$. The most salient feature of these data is the linear variation in \hat{C}_M with louver opening within a range of about $\pm 12\%$ (positive change corresponds to nose up) ostensibly due to the reduction in suction pressure which also leads to reduction in lift. It is also noteworthy that \hat{C}_M data collapse on a single curve, indicating that at least within the range of angles of attack considered here, the fractional increments are independent of α . As shown in Figure IV.1a, the lift decreases linearly with increasing A indicating that the flux of counterclockwise vorticity from the pressure side to the suction side leads to a reduction in lift. The effectiveness of the actuation as measured by the change in lift decreases with increasing angle of attack ostensibly owing to the increase in the thickness of the boundary layer on the suction surface. As noted in Figures IV.1a and b, both the lift and pitching moment can be increased or decreased relative to a trim operating point within

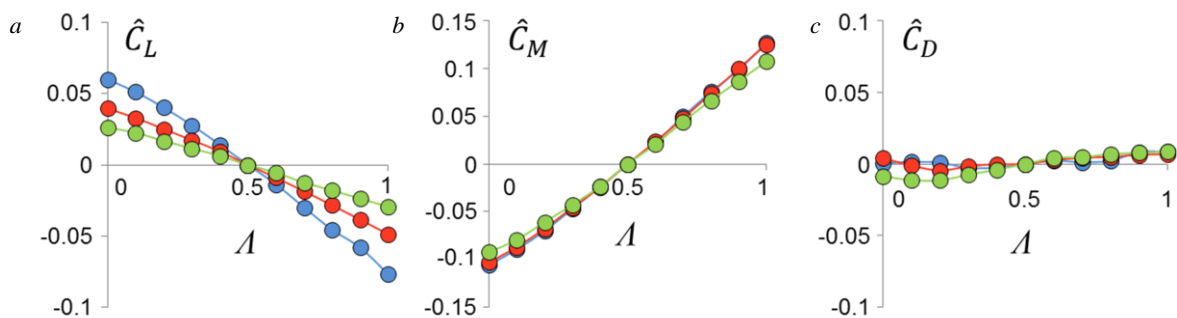


Figure IV.1. Variation of normalized lift (a), pitching moment (b), and drag (c) with fractional opening of the louvers relative to an operating point at 50% louver actuation ($A = 0.5$): $\alpha = 4^\circ$ (●), 8° (●), and 12° (●).

the range of the louvers to mimic the operation of a moving control surface. It is remarkable that the changes in C_M and C_L are accompanied by small changes in drag (up to $\pm 1.6\%$).

IV.2. Immersed Boundary Method

In the immersed boundary method (IB method), surfaces are replaced by a set of Lagrangian points where singular forces are applied to the fluid to enforce the no-slip boundary condition on the surface (see Peskin, 2002, and Mittal and Iaccarino, 2005 for comprehensive reviews of the IB method). Typically, the fluid problem is solved on an Eulerian grid that does not conform to the shape of the body and for simplicity a Cartesian grid is usually employed. Due to the ease of the Eulerian grids, implementation complexity is greatly reduced and more sophisticated methods for speeding up simulations can be used.

The present application employs the formulation presented in Taira and Colonius (2007) and Colonius and Taira (2007) which can be summarized as follows. The non-dimensional Navier-Stokes equations in the presence of a singular boundary force take the form

$$\frac{d\mathbf{u}}{dt} + \mathbf{u} \cdot \nabla \mathbf{u} = -\nabla p + \frac{1}{Re} \nabla^2 \mathbf{u} + \mathbf{f} \quad (\text{IV.2.1})$$

$$\nabla \cdot \mathbf{u} = 0 \quad (\text{IV.2.2})$$

$$\mathbf{U}_B(s, t) = \mathbf{u}(\boldsymbol{\xi}(s, t)) = \int_{\mathbf{x}} \mathbf{u}(\mathbf{x}) \delta(\mathbf{x} - \boldsymbol{\xi}) d\mathbf{x} \quad (\text{IV.2.3})$$

$$\mathbf{f}(\mathbf{x}) = \int_s \mathbf{F}(s, t) \delta(\boldsymbol{\xi} - \mathbf{x}) ds \quad (\text{IV.2.4})$$

where Eq. (IV.2.3) represents the no-slip boundary condition applied at the boundary and Eq.(IV.2.4) is the singular forcing on the boundary. Equation (IV.2.3) is an interpolation of an Eulerian velocity onto the Lagrangian body points. Note that the representation of Eulerian boundary force \mathbf{f} in Eq. (IV.2.1) still includes a delta function-like singularity although its Lagrangian counterpart $\mathbf{F}(s, t)$ is bounded on the surface. Equation (IV.2.4) is the transfer of the boundary force on the Lagrangian points to the Eulerian grid. Despite the singular nature this forcing, in numerical implementation this delta function is replaced by a discrete delta function that essentially smears (regularizes) the singular forcing on the boundary.

The mathematical problem presented in Eqs. (IV.2.1-IV.2.4) is placed in the streamfunction-vorticity formulation by taking the curl of the equations. Numerically, the discrete curl is used to eliminate the pressure and satisfy continuity exactly (see Chang et al., 2002). It is then observed that the usage of the discrete delta function to both interpolate the velocities and regularize the forces gives a specific discrete form of the equations of motion. This specific form allows the Lagrangian forces to be regarded as a set of Lagrange multipliers much like the pressure variables in a classical fractional step method. In doing so, the fractional step method is applied to satisfy the boundary conditions (Eq. IV.2.3) to machine precision, which is analogous to using the pressure variables to satisfy continuity (Eq. IV.2.2, see Perot, 1993).

Boundary conditions remain a problem for the streamfunction formulation. In this application a far-field multi-domain approach is used to reduce the effects of the far-field boundary conditions on the near-field flow. This method is also amenable for using uniform grids since the finest/near-field grid can fit snugly around the immersed boundary points. The vorticity equation can be solved rather efficiently when uniform grids are used in conjunction with simple boundary conditions by taking advantage of the fast Fourier transform (Press et al., 1992). This

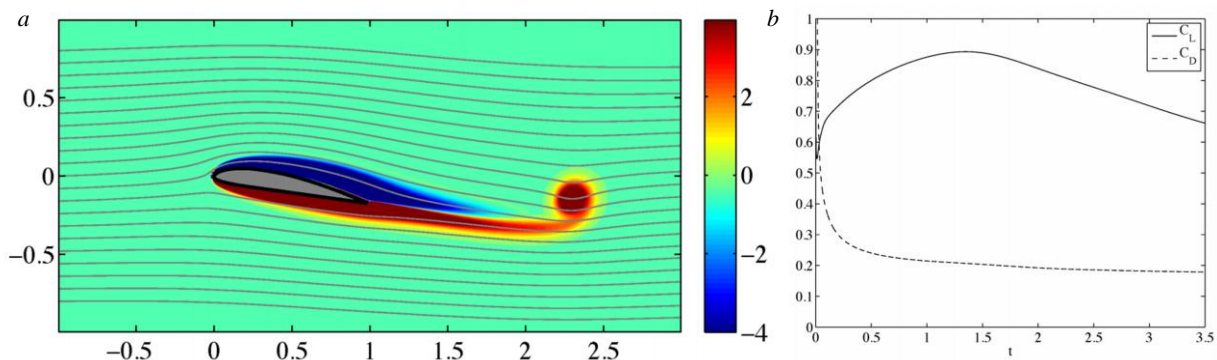


Figure IV.2. A sample calculation of flow over a Clark-Y airfoil at $Re = 1000$ at angle of attack of 10° . Flow is started impulsively from left to right, and vorticity contours and streamlines are shown (a). The decrease of lift is due to a separation bubble forming on the rear of the airfoil. Lift and drag coefficient versus Ut/c (b).

method greatly reduces the required computational cost of the method. See Colonius and Taira (2007) for more details on the multi-domain approach.

When the spacing between the Lagrangian points is constant, forces and moments can be computed by adding the individual boundary forces on the surface and scaling by an arc length parameter. An example calculation of flow variables and forces for an impulsively started Clark-Y airfoil is given in Figure IV.2.

The initial set of bleed laboratory experiments used the Clark-Y airfoil modified to include an internal bleed channel. The corresponding computational geometry is shown in Figure IV.3. Note that the porous surface on the pressure side of the experimental airfoil is modeled as an opening on the pressure side of the computational foil spanning $0.15 \leq x/c \leq 0.19$.

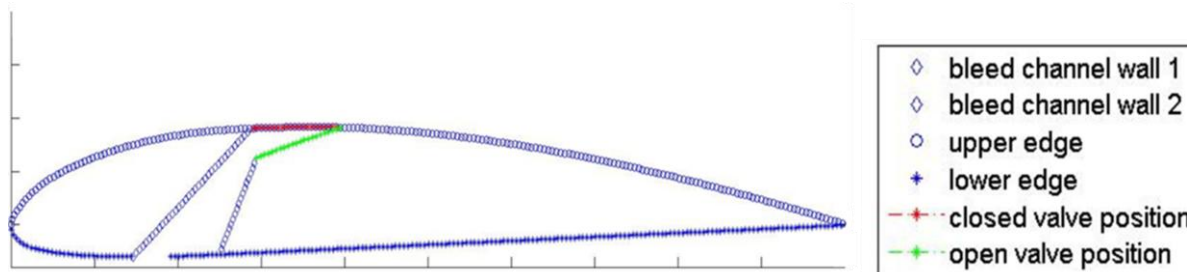


Figure IV.3. Discretized computational model (node spacing of 0.005) of the Clark-Y airfoil used in the numerical simulations of induced bleed.

The application of the IB method is limited to a few cases. Most notable of those is the simulation of unsteady bleed at $\alpha = 20^\circ$. After the initial transients have past, the bleed slot is opened and closed for three cycles as shown in Figure IV.4 along with corresponding unsteady lift and drag. At this modest $Re = 1000$, vortex shedding is clearly defined (Figure IV.5) with a Strouhal frequency $fc/U \cong 0.3$. The imposed valve opening frequency is approximately one-half the shedding frequency, Figure IV.4b. Note that during unsteady valve operation the peak lift is increased by 6-7%, a phenomenon observed in the experiments for leading-edge bleed (to be discussed later). Note also that the lift peaks occur approximately when the valve is completely

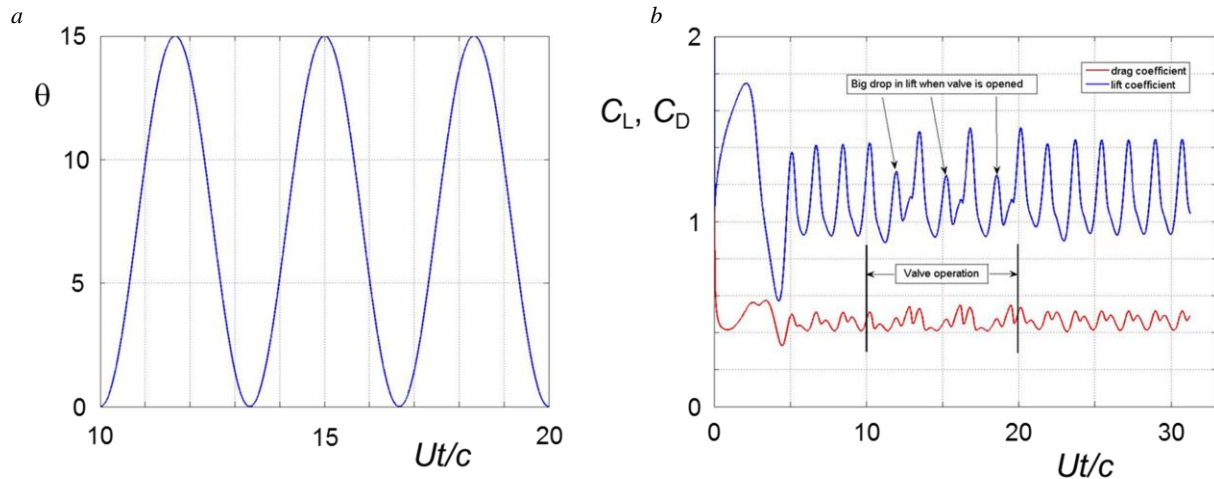


Figure IV.4. Simulated flow past a Clark-Y airfoil at $Re = 1000$ at 20° . Unsteady bleed valve operation during $10 \leq Ut/c \leq 20$. Valve motion during unsteady bleed operation (a), and C_L (blue) and C_D (red) vs. Ut/c (b).

closed during each cycle at $Ut/c = 13.3, 16.6,$ and 20 . The delay presumably corresponds to the time required for the motion of the vortices to produce a higher lift configuration. See Figure IV.5.

For using the IB method in future work it would be necessary to devise a method to calculate the pressure field. Specifically, the pressure distribution is needed on the surface of the airfoil to observe the changes in pressure over the surface. Since the pressure is eliminated in the streamfunction-vorticity formulation, an additional Poisson's equation has to be solved to recover the pressure, i.e.

$$\nabla^2 p = \nabla \cdot \mathbf{f} - \nabla \cdot (\mathbf{u} \cdot \nabla \mathbf{u}). \quad (\text{IV.2.5})$$

This would be done as a post-processing step since the pressure is not needed to advance the simulation in time. It should be pointed out that the specific case of determining the correct pressure on the surface may be difficult due to the nature of the pointwise force singularities on

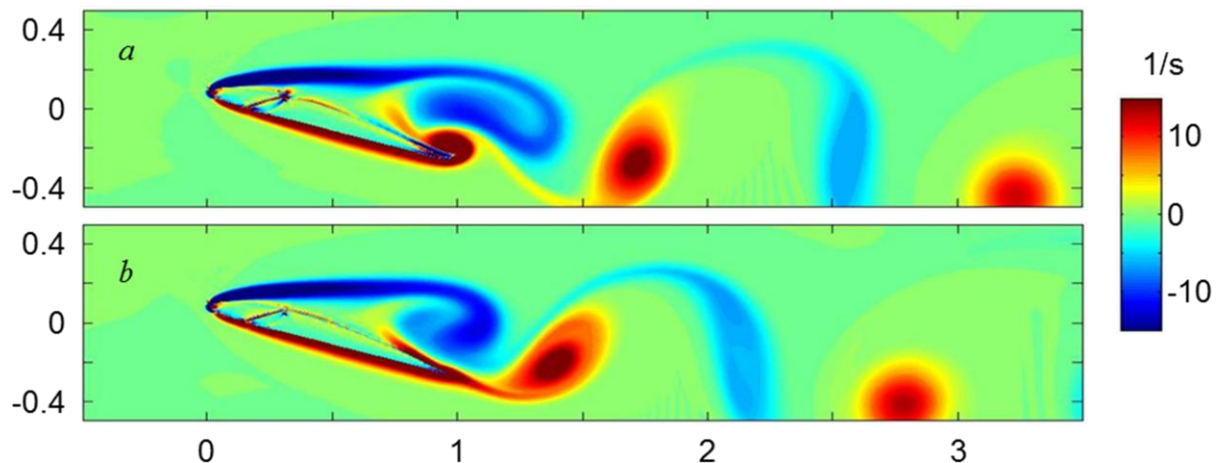


Figure IV.5. Vorticity plots for unsteady bleed. Valve approximately half open, $Ut/c = 12.5$ (a), and valve approximately closed, $Ut/c = 13.75$ (b).

the surface. Along the surface, the pressure field may be expected to contain some oscillations from point to point.

However, the present implementation of the IB method and available computational resources limited simulations to $Re \approx 2500$ or less. Thus, rather than pursuing the above-mentioned extension of the IB method attention was focused on the penalty method assimilation technique as described in the §IV.3.

IV.3. Penalty Method

Another technique used to simulate flows in and around bodies with complex geometries imbedded in a regular mesh is the Brinkman penalization method (Angot et al., 1999, and Arquis and Caltagirone, 1984). In this method the force term

$$\mathbf{f} = -\frac{1}{\eta}\chi_s\mathbf{u} \quad (\text{IV.3.1})$$

is used on the RHS of the momentum equation, Eq. (IV.2.1), where $\eta \geq 0$ is the penalization coefficient and $\chi_s(\mathbf{x}, t)$ is the characteristic function of the body, i. e.,

$$\begin{aligned} \chi_s(\mathbf{x}, t) &= 1 \text{ if } \mathbf{x} \text{ is in the body,} \\ &= 0 \text{ if } \mathbf{x} \text{ is in the fluid.} \end{aligned} \quad (\text{IV.3.2})$$

In such a scheme the force given by Eq. (IV.3.1) replaces the no-slip condition and it has been shown (Angot et al., 1999) that as $\eta \rightarrow 0$ the solution to the penalization method converges to the solution to the Navier-Stokes equations with no-slip boundary conditions. The present implementation uses the vorticity-velocity form of the Navier-Stokes equations. Therefore the vorticity transport equation will have on the RHS the vorticity source term $-\frac{1}{\eta}\nabla \times [\chi_s\mathbf{u}]$, i.e., the curl of the RHS of Eq. (IV.3.1).

In practice one has to choose a nonzero η and a particular discretization of the characteristic function $\chi_s(\mathbf{x}, t)$. In addition, because the penalty force is local, either a very small timestep or a series of iterations between timesteps is required because the effects of the no-slip condition are nonlocal for an incompressible flow. For the simulations in this study using the penalty a hybrid re-meshed vortex particle method is used to solve the vorticity transport equation. In addition the mesh is refined locally as needed, e.g., near the airfoil and in the bleed slots, employing a wavelet-based procedure. The simulations were performed on GPU (graphics processor unit) accelerated CPUs. As a result of the above, flows past bodies with complex boundaries at $Re = 10,000$ to $20,000$ could be achieved in a reasonable turnaround time. See Rossinelli et al. (2010) and Gazzola et al. (2011) for further details.

The bleed slot geometry for the experimental studies of trailing-edge bleed on a Clark-Y airfoil is shown in Figure IV.6 while the geometry for the numerical simulations is given in Figures IV.7 and IV.8. The simulations of trailing-edge bleed presented in this section are based on a NACA 4415 airfoil for convenience. Note that in the simulations either one, two,

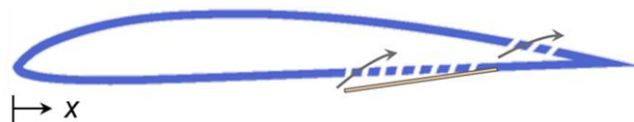


Figure IV.6. Schematic of the modified Clark-Y airfoil used in the experimental investigation of trailing-edge bleed. Each of the bleed openings is $0.0165c$ wide. Eight pressure-side ports are located at $x/c = 0.596, 0.632, 0.665, 0.697, 0.729, 0.761, 0.789, \text{ and } 0.816$. Three suction-side ports are located at $x/c = 0.764, 0.802, \text{ and } 0.837$.

or three bleed channels are employed, each with varying inlet widths providing nine bleed configurations as shown.

Vorticity fields for two bleed configurations are shown in Figure IV.9. The presence of bleed is accompanied by loss in lift but also an additional pitch-up moment (c.f. Figure IV.1). The results of a sample of three of the many simulations that were run are shown in Figure IV.10. The cases shown are the flow past an airfoil at 6° after an impulsive start. There are two low-bleed cases and one with no bleed, all at $Re = 9,500$. By averaging $C_L(T)$ and $C_M(T)$ over the time interval $0 \leq T = U t/c \leq 5$ the mean values for C_L and C_M , respectively, are obtained for each case. For each case with nonzero bleed ΔC_L is defined as the mean C_L for that bleed case

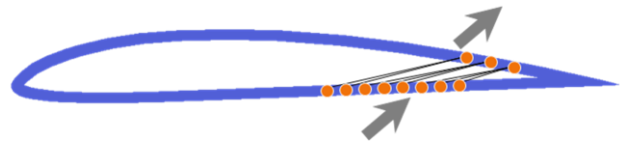


Figure IV.7. Computational bleed model for simulations of trailing-edge bleed. Inlet and outlet locations and sizes are the same as those in the experimental airfoil.

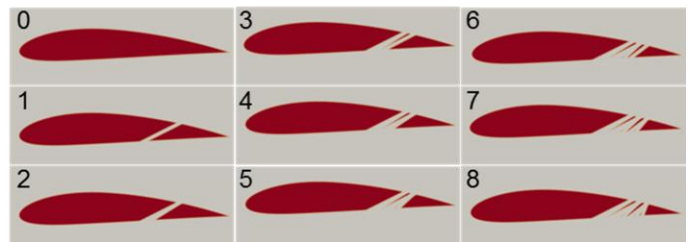


Figure IV.8. Nine bleed configurations studied in the simulations of trailing-edge bleed.

minus the mean C_L for the corresponding no-bleed case, i.e., same angle of attack but bleed configuration 0. The same procedure is used to compute ΔC_M . Shown at the bottom right of Figure IV.10 is the resulting ΔC_L vs. ΔC_M for the three cases covered in this figure.

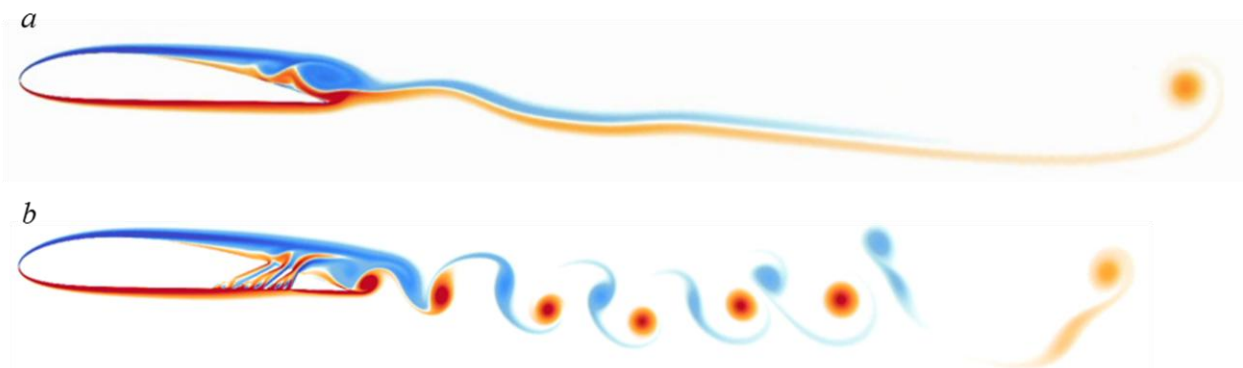


Figure IV.9. Vorticity plots for the simulated flow past a NACA 4415 airfoil at $Re = 9500$, $\alpha = 4^\circ$, with bleed slots closed in configuration 0 (a), and with bleed slots fully open in configuration 8 (b).

Similar simulations were performed for 36 cases, four angles of attack (0° , 2° , 4° , and 6°), each with nine different bleed configurations as shown in Figure IV.8. The resultant ΔC_L vs. ΔC_M plot is shown in Figure IV.11 along with the results of experimental cases as described in Figure IV.1. Note that:

- The results, computational and experimental, show that $\Delta C_M \approx -1/7 \Delta C_L$ for all trailing-edge bleed configurations and all low to moderate angles of attack studied. This fact is an essential ingredient in the reduced-order model described in the next section.
- The largest lift and moment changes observed experimentally are achieved with just the low-bleed configurations 2 or 3 in the simulations, implying that if higher porosities could be

achieved experimentally, then concomitant higher lift and moment changes could be achieved as well.

- The experimental results show very little dependence of ΔC_L and ΔC_M on angle of attack, whereas the simulations produce higher lift and moment changes as the angle of attack increases.

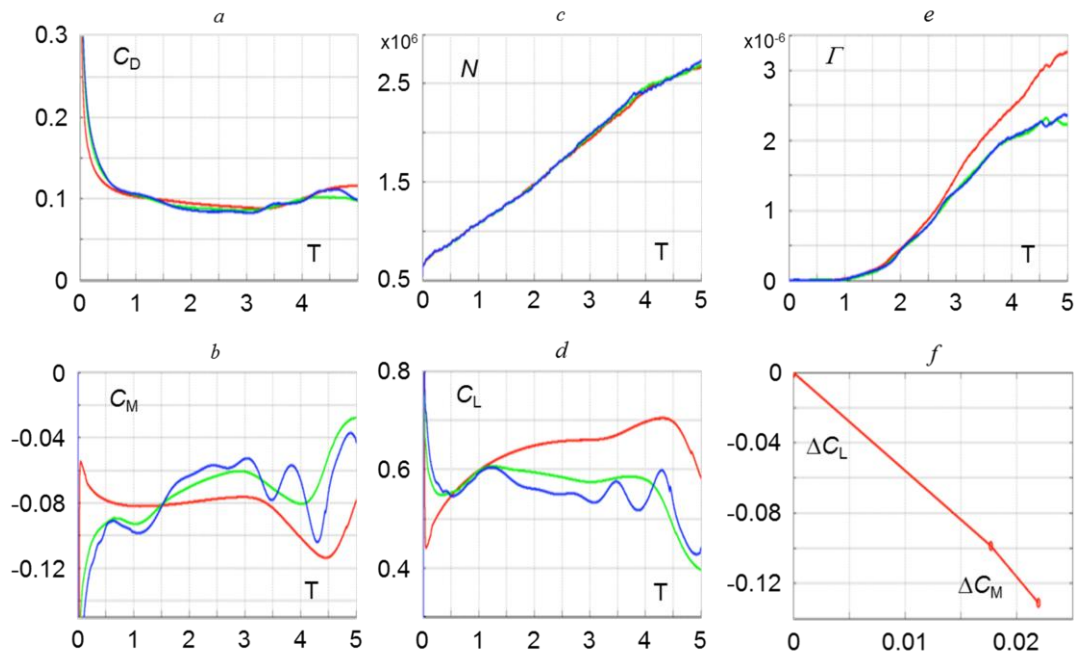


Figure IV.10. Impulsively started flow past a NACA 4415 airfoil at $\alpha = 6^\circ$, $Re = 9500$ for no bleed (red), with bleed configuration 1 (green), and with bleed configuration 2 (blue). C_D vs. $T = Ut/c$ (a), C_M vs. T (b), Number of vortex elements vs. T (c), C_L vs. T (d), Circulation in the computational domain vs. T (e), and ΔC_L vs. ΔC_M (f) for the three cases in this figure.

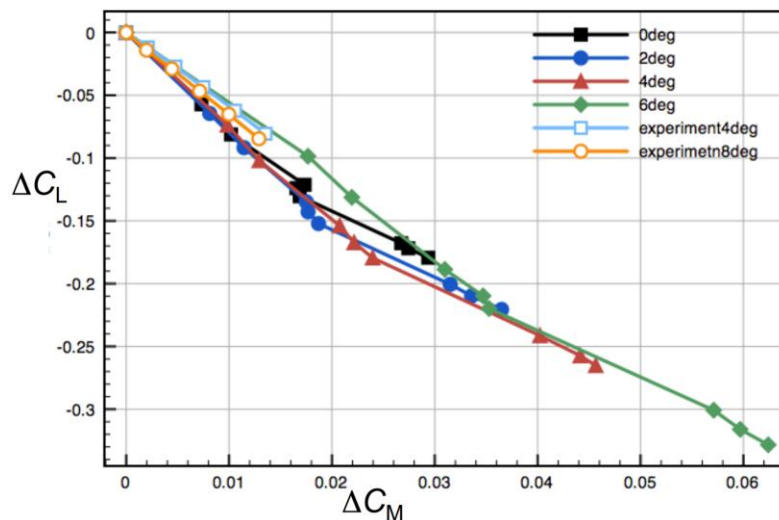


Figure IV.11. Change in lift versus change in pitching moment due to trailing edge bleed.

The simulations described in this section and the previous one are two-dimensional and at relatively low Re compared to experiment so that discrepancies between the two should not be surprising. Clearly it would have been preferable to do the computations in three dimensions with large-eddy simulations but this entails a major effort, beyond the scope of this computational/theoretical study.

IV.4. Vortex Reduced Order Model

The development of a vortex reduced order model (ROM) is based on the modification and extension of an existing flat-plate model (Tchieu and Leonard, 2007) for a pitching, plunging airfoil to include active bleed. The vorticity in the model consists of freely-moving vortices in the wake and boundary-layer vorticity on the airfoil surface. Small-amplitude motions of a flat-plate airfoil which lead to a number of simplifying assumptions are considered. Thus, for example, all but one of the wake vortices move uniformly downstream along the nominal x -axis that is fixed to the airfoil. The exception is the vortex being fed circulation from the trailing edge. The velocity of the latter vortex is modified to conserve momentum. In addition it is assumed that:

- Vorticity is shed into the wake to satisfy the unsteady Kutta condition (no velocity singularity) at the trailing edge.
- A vortex sheet with a continuous distribution of vorticity is used to satisfy the boundary condition on the airfoil surface (normal component of velocity is continuous) plus the Kutta condition.
- Aero-bleed is achieved through sources and sinks on the surface of the plate.
- Lift and moment are computed from the time-derivative of the fluid impulse and the angular impulse, respectively, plus a bleed contribution.

Consider an airfoil of chord length c occupying the portion $-c/2 \leq x \leq c/2$ of the x -axis. The airfoil is undergoing small-amplitude motions in pitch and plunge.

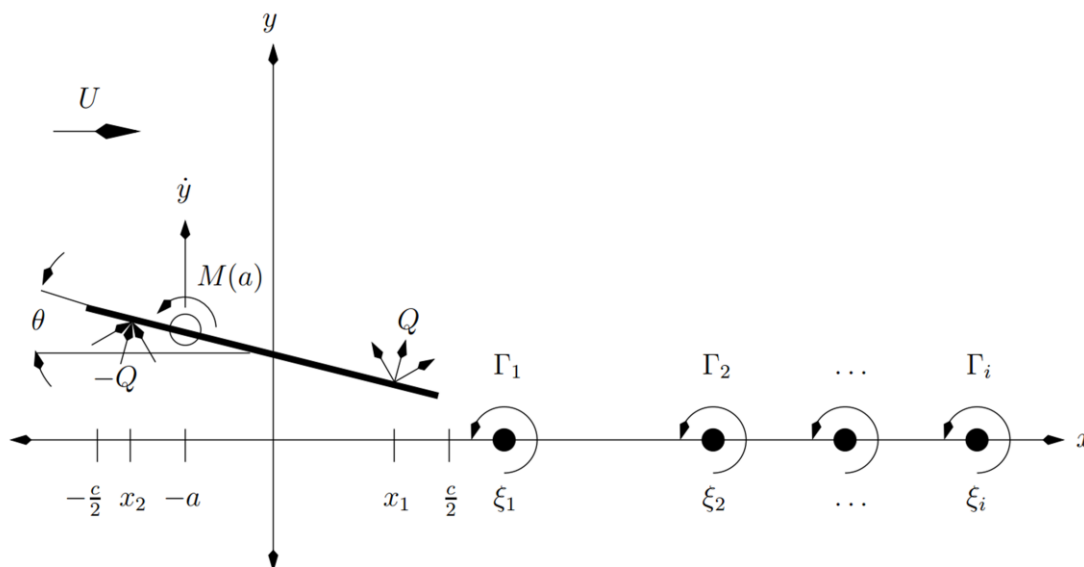


Figure IV.12. Pitching, plunging airfoil, wake vortices with strengths Γ_i , $i = 1, \dots, N$, and a time-dependent source Q at x_1 and sink $-Q$ at x_2 .

located at $x = -a$ as shown in Figure IV.12. The airfoil velocity is U in the $-x$ direction. (Alternatively, one could apply the results below to a stationary airfoil with a freestream velocity U in the $+x$ direction.) The volume flow rate or bleed through the airfoil is Q . Only one source location and one sink location are assumed for simplicity but the extension to multiple source and sink locations is straightforward.

IV.5. Vortex ROM I

The initial extension of the previous analysis to include bleed shows that the steady state lift coefficient is augmented by

$$\Delta C_L = \frac{2Q}{\pi U c} [F(2x_1/c) + F(2x_2/c)] \quad (\text{IV.5.1})$$

and the steady state (pitch up) moment coefficient by

$$\Delta C_M = -\frac{a}{c} \Delta C_L + \frac{Q}{\pi} [G(2x_1/c) - G(2x_2/c)] \quad (\text{IV.5.2})$$

where $F(z) = \sqrt{(1+z)/(1-z)}$ and $G(z) = z \log[(1+z)/(1-z)]$.

The above results are based on the assumption that the source and sink are isotropic and that there is no interaction between the bleed and the boundary layers on the airfoil. However, the louver geometry of the experiments and boundary layer interactions will most likely produce a source flow that is predominately directed downstream. Another additional force term

$$\Delta \mathbf{F} = \rho \oint_S \mathbf{n} \cdot (\mathbf{u} - \mathbf{u}_s) \mathbf{u} dS \quad (\text{IV.5.3})$$

depending directly on bleed, may come into play. In addition, the airfoil boundary layer on the bleed outlet side will thicken, affecting the pressure gradient at that point.

To implement the above model, Eqs. (IV.5.1) and (IV.5.2), one would also have to develop an expression for Q as a function of angle of attack, bleed geometry, etc. Before embarking on such a task, the above model is tested using the results of experimental static bleed cases with measured values of Q . It is found that the model consistently underpredicts the changes in lift and drag due to bleed by about a factor of four. Thus, a new approach to modeling the effects of bleed is developed as described in §IV.6.

IV.6. Vortex ROM II

To initiate the new approach to modeling, experimentally observed changes in pressure distributions along a static airfoil due to steady bleed are examined. Ten cases with varying amounts of bleed are shown in Figure IV.13. In general, the positive changes in C_p shown occur on the suction side while negative changes occur on the pressure side.

The interaction between the bleed and the cross flow is investigated using PIV. Figure IV.14 shows images of the flow from approximately $x/c = 0.65$ to $0.1c$ beyond the trailing edge in the cross stream (x - y) plane for $\alpha = 4^\circ$ (the bleed orifices are marked). The effects of the bleed for $A = 0$ and 1 are shown in Figures IV.14a and b respectively. When the louvers are open, the boundary layer on the suction surface becomes significantly thicker, resulting in cross stream spreading of the near wake. Figure IV.14c shows the “residual” velocity (i.e. $A = 1$ relative to $A = 0$) and illustrates the decrease in velocity due to bleed. These data indicate that the bleed

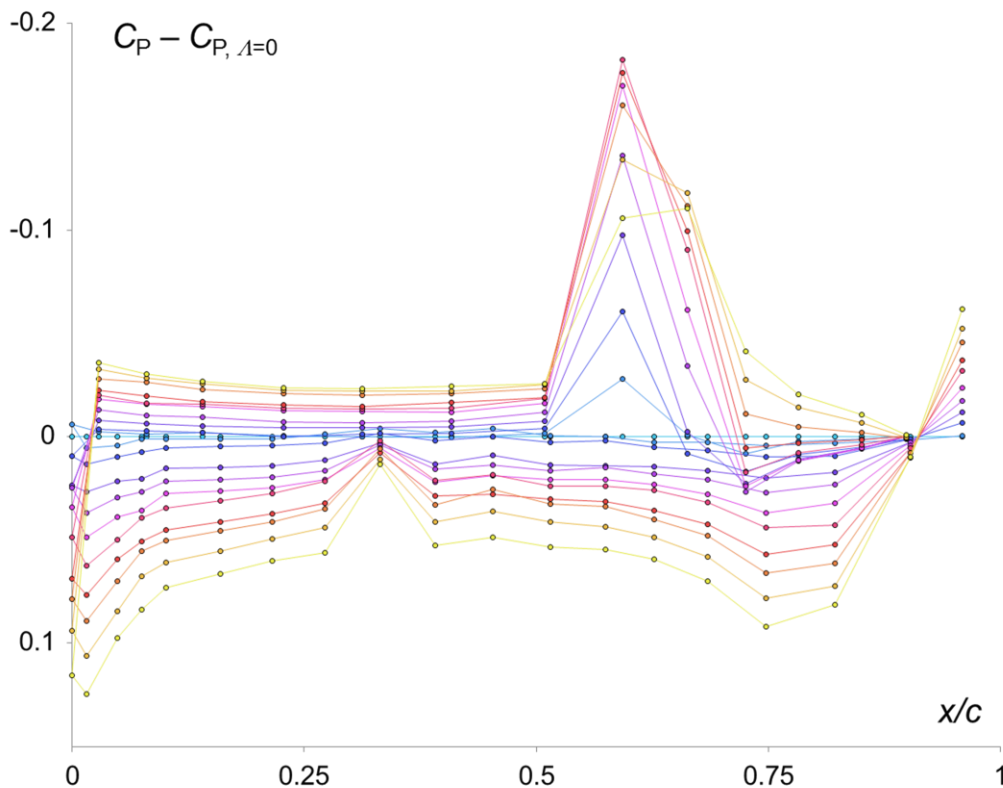


Figure IV.13. Experimental change in pressure distribution due to bleed, $\alpha = 8^\circ$. Ten levels of bleed shown: $\Lambda = 0.1$ (●), 0.2 (●), 0.3 (●), 0.4 (●), 0.5 (●), 0.6 (●), 0.7 (●), 0.8 (●), 0.9 (●), and 1 (●).

results primarily in cross stream spreading of the suction side boundary layer but does not accelerate the outer flow or result in turning of the near wake. Exploiting bleed to control the flow velocity in the boundary layer alters the local suction and thereby induces nose-up or nose-down pitching. It is notable that, relative to a partial-bleed configuration (e.g. $\Lambda = 0.5$), significant variations in C_M can be attained directly by increasing or decreasing the bleed level, which enables maneuvering in pitch without the use of external control surfaces.

Note in particular the negative peak on the pressure side of Figure IV.13 extending approximately $0.55 \leq x/c \leq 0.75$ due to presence of the inlet bleed flow and the positive bulge in pressure towards the trailing edge on the suction side due to boundary-layer thickening in Figure IV.14. Together, these effects due to bleed are termed as *Local*. Note also that substantial changes in pressure occur on the forward portion of the airfoil away from the bleed slots. These latter changes correspond to changes in airfoil circulation that are required to maintain the Kutta condition at the trailing edge. This effect is termed as global or *Kutta*. (The dip in ΔC_P on the suction side ahead of midchord is quite likely due to a malfunctioning pressure tap near $x/c = 0.35$.)

For modeling purposes, it is necessary to determine the components of lift due to local effects and Kutta effects separately. In addition, the center of pressure must be determined for ΔC_P^{local} local. To start, consider the net change in pressure distribution due to bleed, $\Delta C_{PSS}(x/c) - \Delta C_{PPS}(x/c)$, shown in Figure IV.15a for the 8° case where the differences are for full bleed minus no bleed.

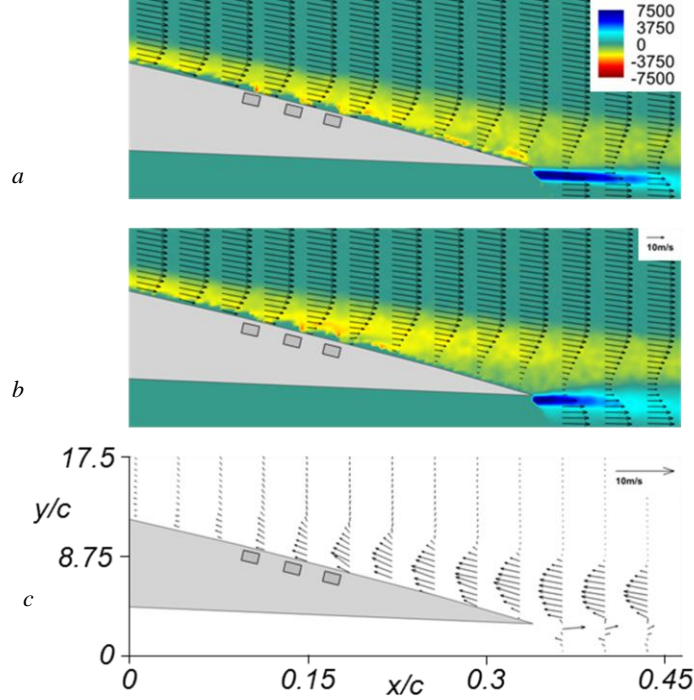


Figure IV.14. Bleed through the trailing edge orifices (gray), showing vorticity concentrations and velocity vectors for (a) $\Lambda = 0$, (b) $\Lambda = 1$, and (c) the residual velocity.

For a static flat-plate airfoil with a change in lift of ΔC_L , this quantity is given by (e.g., von Kármán and Sears (1938) plus use of the linearized Bernoulli equation)

$$\Delta C_{PSS}(x/c) - \Delta C_{PPS}(x/c) = \frac{2}{\pi} \sqrt{\left(\frac{1-x/c}{x/c}\right)} \Delta C_L \quad (\text{IV.6.1})$$

Thus the change in Kutta lift due to bleed would given in terms the function

$$C_p^*(x/c) = -\frac{\pi}{2} (\Delta C_{PSS}(x/c) - \Delta C_{PPS}(x/c)) \sqrt{\left(\frac{x/c}{1-x/c}\right)} \quad (\text{IV.6.2})$$

i.e., $C_p^*(x/c)$ should be constant and equal to ΔC_L^{Kutta} near the leading edge.

This procedure is used to estimate ΔC_L^{Kutta} as shown in Figure IV.15b. In principle, one should find a flat (horizontal) spot in the curve near the leading edge, revealing ΔC_L^{Kutta} . It appears, however, that the flat-plate approximation is not sufficiently accurate for pressure distributions near the rounded leading edge of a Clark-Y airfoil. The predicted ΔC_L^{Kutta} varies more than 50% in the interval $0.05 \leq x/c \leq 0.28$.

A better scheme is to use the actual net pressure distribution near the leading edge of a Clark-Y airfoil with no bleed as a measure of the lift due to global effects or the Kutta condition. Thus $C_{PSS}(x/c)|_{no\ bleed} - C_{PPS}(x/c)|_{no\ bleed}$ is used along with the corresponding $C_L|_{no\ bleed}$ to estimate ΔC_L^{Kutta} in terms of the function $C_p'(x/c)$, defined by

$$C_p'(x/c) = \frac{\Delta C_{PSS}(x/c) - \Delta C_{PPS}(x/c)}{\Delta C_{PSS}(x/c)|_{no\ bleed} - \Delta C_{PPS}(x/c)|_{no\ bleed}} C_L|_{no\ bleed} \quad (\text{IV.6.3})$$

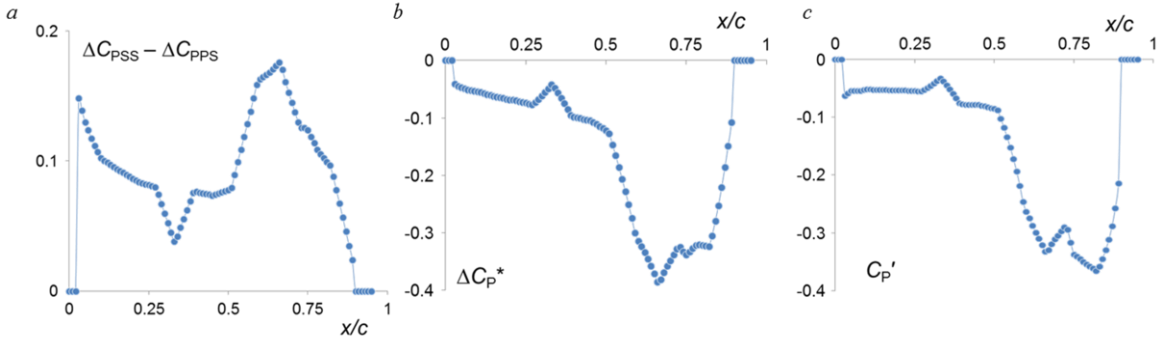


Figure IV.15. Net change in experimental pressure distribution due to bleed, $\Delta C_{PSS}(x/c) - \Delta C_{PPS}(x/c)$, full bleed ($\Lambda = 1$) minus no bleed ($\Lambda = 0$), $\alpha = 8^\circ$ (a). Estimate of ΔC_L^{Kutta} using the flat-plate approximation (b). See text and Eqs. (IV.6.1) and (IV.6.2). Estimate of C_P' using the net pressure distribution from the Clark-Y airfoil no-bleed case (c). See text and Eq. (IV.6.3).

and again, $C_P'(x/c)$ should be constant and equal to ΔC_L^{Kutta} near the leading edge.

The results of this procedure are plotted in Figure IV.15c. Now note, for this case, a relatively unambiguous estimate of ΔC_L^{Kutta} of approximately 0.052 is obtained from the flat portion of the curve between $0.05 \leq x/c \leq 0.28$. The corresponding ΔC_L^{Local} is then

$$\Delta C_L - \Delta C_L^{Kutta} = 0.72 - 0.052 = 0.20.$$

Repeating this procedure on the experimental data for the other nine levels of bleed $\Lambda = 0.1, 0.2, \dots, 0.9$, the results for ΔC_L^{Kutta} and ΔC_L^{Local} are obtained and shown in Figure IV.16.

Note from Figure IV.16 that $\Delta C_L^{Local} \approx 2/5 \Delta C_L^{Kutta} \approx 2/7 \Delta C_L$ is a fair approximation for the data shown with the origin shifted to $\Lambda = 0.1$. This allows computation of the center of pressure of ΔC_L^{Local} as follows. The component of lift corresponding to ΔC_L^{Kutta} acts at quarter chord. Let ξ_B be the center of pressure of ΔC_L^{Local} expressed as a fraction of the chord from the leading edge. Therefore $\Delta C_M = -(\xi_B - 1/4) \Delta C_L^{Local} = -(\xi_B - 1/4) 2/7 \Delta C_L$. Thus, to achieve the result $\Delta C_M = -1/7 \Delta C_L \xi_B$ must be $(3/4)x/c$.

To summarize, trailing-edge bleed affects the quasi-steady distribution of vorticity on the airfoil in two ways. If $\Gamma_B(\Lambda(t))$ is the quasi-steady change in circulation due to bleed, then $\alpha_B \Gamma_B(\Lambda(t))$ is the change related to the Kutta condition and therefore $(1 - \alpha_B) \Gamma_B(\Lambda(t))$ is the change corresponding to the local effect with $\alpha_B = 5/7$ as determined above. The former has a center of pressure at quarter-chord while the latter has a center of pressure at $\xi_B = (3/4)x/c$.

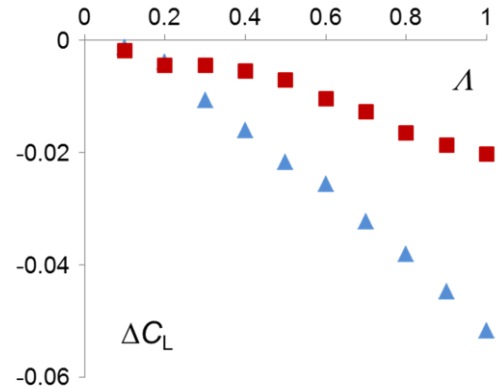


Figure IV.16. ΔC_L^{Kutta} (\blacktriangle) and ΔC_L^{Local} (\blacksquare) as functions of bleed level Λ at $\alpha = 8^\circ$.

Knowing the quasi-steady contributions of circulation on the airfoil allows writing expressions for unsteady lift and moment for the general case (Tchieu and Leonard, 2007) of a pitching, plunging airfoil with unsteady bleed. The lift coefficient is given by

$$C_L = -\pi \left(\frac{c}{2U^2} \ddot{y} + \frac{2}{U} \dot{y} \right) + \pi \left[\frac{ac}{2U^2} \ddot{\theta} + \frac{2a+c}{U} \dot{\theta} + \frac{c\dot{U}+4U^2}{2U^2} \theta \right] - \frac{1}{U} \sum_{i=1}^N \frac{\Gamma_i}{\sqrt{\xi_i^2 - c^2/4}} - \frac{2}{Uc} \Gamma_B(\Lambda(t)) \quad (\text{IV.6.4})$$

and the moment coefficient (with pitch up as positive) is

$$C_M = -\frac{a}{c} C_L - \frac{\pi}{2U} \dot{y} - \pi \left[\frac{c^2}{64U^2} \ddot{\theta} - \frac{a}{2U} \dot{\theta} - \frac{1}{2} \theta \right] - \frac{1}{4U} \sum_{i=1}^N \frac{\Gamma_i}{\sqrt{\xi_i^2 - c^2/4}} + \frac{2\xi_B}{Uc^2} (1 - \alpha_B) \Gamma_B(\Lambda(t)) \quad (\text{IV.6.5})$$

Refer to Figure IV.12 for definitions of the other variables appearing in the above equations. Note that in this version of the ROM no use is made of the source strength Q . Rather, the procedure relies on experimentally determined values of $\Gamma_B(\Lambda)$ (or, equivalently, $\Delta C_L(\Lambda)$), α_B , and ξ_B .

For a closed system of equations, the dynamics of the circulations Γ_i and locations ξ_i of the wake vortices should be specified. All but one of the free vortices in the wake moves with speed U . Thus,

$$\frac{d\xi_i}{dt} = U \quad (i \geq 2), \quad (\text{IV.6.6})$$

and the vortex being fed circulation (labeled $i = 1$) moves with speed

$$\frac{d\xi_1}{dt} = U - \frac{(\xi_1^2 - c^2/4)}{\xi_1 \Gamma_1} \frac{d\Gamma_1}{dt} \quad (\text{IV.6.7})$$

where conservation of impulse was used to derive Eq.(IV.6.7).

Except for the vortex being fed, all vortices in the wake remain at constant circulation:

$$\frac{d\Gamma_i}{dt} = 0 \quad (i \geq 2). \quad (\text{IV.6.8})$$

The strength of Γ_1 is determined from the requirement that the total circulation must equal 0 as follows:

$$\Gamma_B + \Gamma_0 + \sum_{i=1}^N \Gamma_i \sqrt{\frac{\xi_i + c/2}{\xi_i - c/2}} = 0 \quad (\text{IV.6.9})$$

Here Γ_0 is the quasi-steady circulation about the airfoil, excluding bleed effects, that depends only on the pitch angle, its time derivative, and the plunge rate. N is the number of free vortices in the wake. A new vortex is shed, becoming the new $i = 1$ vortex, whenever the current $i = 1$ vortex would decrease in amplitude in the next instant of time, thus satisfying the physical constraint that $\Gamma_1(t)$ never decreases in magnitude. Refer to Tchieu and Leonard (2007) for further details.

In the above ROM it is assumed that the quasi-steady circulation due to bleed Γ_B is established during a timescale that is much smaller than those of any of the dynamical effects of interest. If this not the case, a dynamical equation relating $\Gamma_B(t)$ to $A(t)$ would be needed.

V. LEADING EDGE BLEED ACTUATION, STATIC AIRFOIL

V.1. Steady Bleed Actuation

At moderate and high angles of attack, bleed actuation is applied on the suction side near the leading edge ($0.03 < x/c < 0.07$), where the bleed is controlled by the louvers on the pressure side near the trailing edge (cf. Figure II.6b). The variation of the lift coefficient with angle of attack is shown in Figure V.1 for several louver openings and for the sealed airfoil. For this configuration, louver actuation is mostly effective between 8° and 20° and is manifested by a large change in lift with a maximum $\Delta C_L = 0.7$ at $\alpha = 16^\circ$. As shown in Figure V.1b, these changes in lift are accompanied by a small penalty in drag, with a maximum excursion of 0.1 from the baseline C_D for $8^\circ < \alpha < 20^\circ$. Leading edge bleed leads to a small nose-up pitching moment relative to the baseline for all bleed levels up $\alpha = 8^\circ$, and actuation at higher angles primarily leads to a stronger negative moment with a maximum magnitude of $\Delta C_M = 0.061$ at $\alpha = 14^\circ$, or 85% of the baseline value. It is also interesting that, over the range $10^\circ < \alpha < 12^\circ$, varying actuation can yield a nose-up or nose-down moment relative to the baseline, which allows a degree of maneuvering control based solely on bleed flow. The variation in C_L with A indicates that lift can be varied relative to some “operating point” that can be set within the range of louver opening. Then, the local sectional lift of the airfoil can be either increased or decreased relative to this operating point by modifying the spanwise variation of the bleed, without external control surfaces. In addition to aerodynamic maneuvering (for example roll by differential spanwise lift), this approach can be used for direct lift control (DLC) during landing and stabilization of light, flexible airframes that are used for high-altitude UAVs.

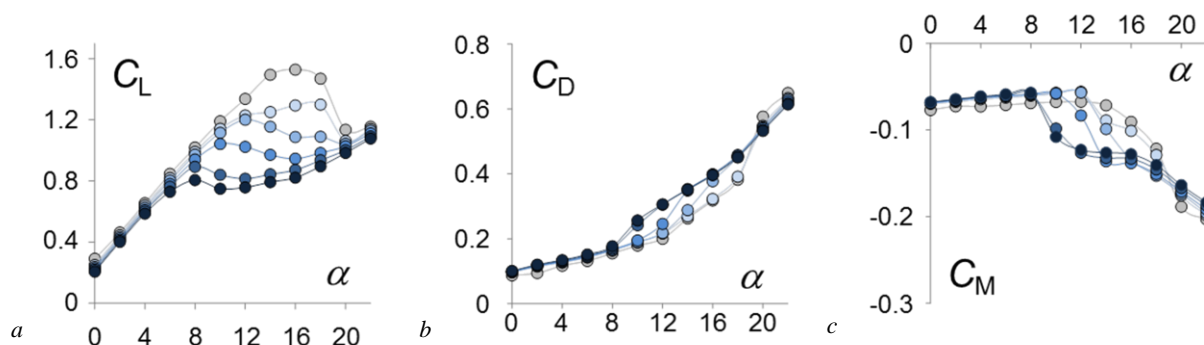


Figure V.1. Variation of lift (a), drag (b), and pitching moment (c) with angle of attack for different stationary louver openings: baseline airfoil (\circ), and $\Lambda = 0$ (\circ), 0.25 (\circ), 0.5 (\circ), 0.75 (\circ), and 1 (\bullet).

The interaction between the bleed flow and cross flow near the surface on the suction side of the airfoil is investigated using PIV as shown in Figure V.2 ($\alpha = 18^\circ$ $Re = 190,000$), where the field of view measures $0.175c \times 0.075c$ in the cross stream directions (shown schematically in the inset). The figure includes color raster plots of the vorticity concentrations (superposed with velocity vectors, Figures V.2a-e), turbulent kinetic energy (TKE, Figures V.2f-j), and vector

distributions of “residual” velocity that shows the local velocity differences between the flow fields in the presence and absence of bleed (Figures V.2k-n). These data are obtained for $\Lambda = 0, 0.25, 0.5, 0.75,$ and 1 for which the momentum coefficients of the bleed jet are $C_{\mu} = 0.63 \cdot 10^{-4}, 1.24 \cdot 10^{-4}, 1.24 \cdot 10^{-4}, 1.87 \cdot 10^{-4}, 4.43 \cdot 10^{-4},$ and $5.47 \cdot 10^{-4}$, respectively (note that C_{μ} is estimated from PIV measurements of the jets’ volume flow rates, c.f. Figure V.3 below).

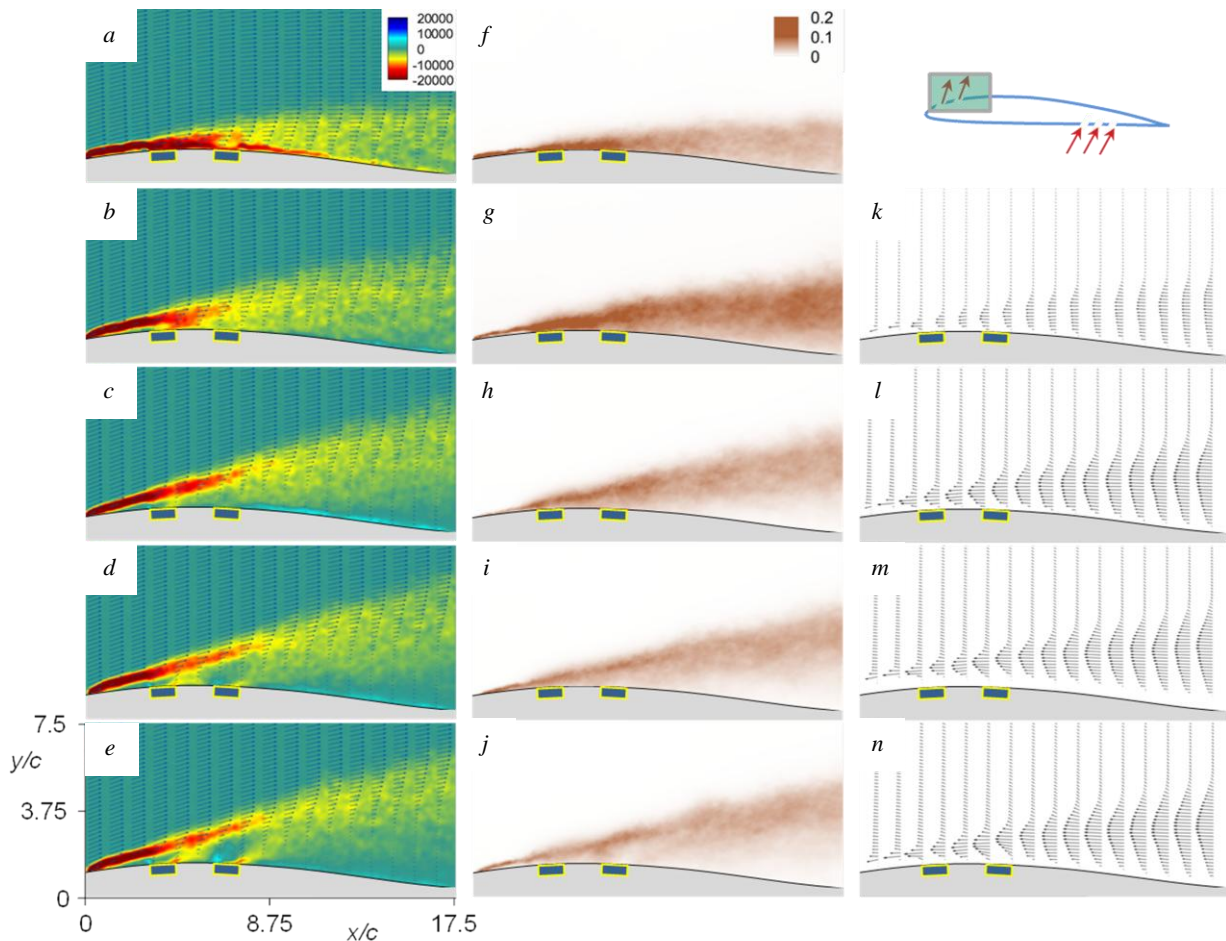


Figure V.2. The interaction between the bleed and the cross flow near the suction surface within the field of view shown schematically in the inset (top right): (a-e) are distributions of velocity vectors and vorticity concentrations for $\Lambda = 0$ (a), 0.25 (b), 0.50 (c), 0.75 , (d), and 1 (e); (f-j) are corresponding distributions of TKE; and (k-n) are the corresponding residual velocities.

In the absence of bleed ($\Lambda = 0$, Figure V.2a), the flow is nominally attached to the airfoil in the vicinity of the open bleed orifices on the suction surface (marked on the image). It is evident that small perturbations associated with the presence of the orifices lead to some thickening of the boundary layer. As the bleed commences ($\Lambda = 0.25$, Figure V.2b), the flow separates locally from the surface at $x/c = 0.10$. At this bleed level, the separation domain within the field of view (as assessed from the presence of the reversed flow in Figure V.2k) is relatively shallow and the corresponding raster plot of TKE (Figure V.2g) shows a central streamwise band of higher TKE that is bounded by lower intensity bands along the surface of the airfoil and near the outer flow. When $\Lambda = 0.5$ (Figure V.2c), the separating shear layer is lifted farther away from the surface

with a distinct domain of lower-level spanwise vorticity concentrations near the surface of the airfoil. As shown by the residual velocity (Figure V.2l), the domain of reversed flow begins upstream of the first bleed port ostensibly owing to local blockage. It is remarkable that even though the momentum coefficient of the bleed is small ($C_\mu = 1.87 \cdot 10^{-4}$), it is sufficient to displace the oncoming flow and result in stronger separation as is evidenced by the extended streamwise domain of intense clockwise vorticity within the core of the separating shear layer. It is noteworthy that the intensity of TKE within the separating shear layer (Figure V.2h) is somewhat lower than for $\Lambda = 0.25$ (Figure V.2g) indicating lower turbulence production as the shear layer spreads in the cross stream direction. Further increase in the bleed ($\Lambda = 0.75$ and 1) is marked by the intensification of the bleed jets out of both ports (Figures V.2d and e), but the induced changes in the separated flow within the field of view are rather subtle and the increase in spreading of the shear layer into the free stream is minimal, as is also evidenced in the corresponding plots of TKE (Figures V.2i and j) and residual velocity (Figures V.2m and n). A measure of the cross stream spreading of the separating shear layer at the downstream edge of the field of view is obtained by considering the cross stream elevation where the magnitude of the residual velocity is about 20% of the free stream speed. This elevation increases with Λ to $0.045c$ ($\Lambda = 0.25$), $0.061c$ ($\Lambda = 0.5$), $0.065c$ ($\Lambda = 0.75$), and $0.072c$ ($\Lambda = 1$). Recall that these changes correspond to significant decrements in C_L as shown in Figure V.1a, although the magnitude of the rate of change of C_L with Λ [0.26 ($\Lambda = 0.25$), 0.19 ($\Lambda = 0.5$), 0.17 ($\Lambda = 0.75$), and 0.15 ($\Lambda = 1$)] decreases as Λ is increased, which is commensurate with corresponding slowdown in the cross stream growth of the separated flow domain.

The bleed flow is clearly visible in Figures V.2b-e. As noted above, the onset of the separating shear layer is upstream of the first bleed port ($x/c = 0.03$), and the bleed flow layers merge with the shear layer farther downstream as Λ (and C_μ) is increased. It is interesting to note that the sense of the vorticity concentration within the bleed flow is predominantly clockwise, indicating that the interaction with the reversed flow near the surface of the airfoil is weak at best. Since the bleed flow is driven by the pressure difference across the bleed ports, it is also remarkable that even though stall decreases the magnitude of that pressure difference, the bleed intensifies with fractional opening, suggesting that the interaction with the separating shear layer (cf. Figure V.2e) is stronger owing to the lower speed of the cross flow in the vicinity of the bleed ports.

The PIV data in Figure V.2 are used to quantify the volume flow rate of the bleed (Figure V.3a), the bleed nominal momentum coefficient C_μ (Figure V.3b), and the cross-stream vorticity thickness of the separating shear layer δ_ζ (Figure V.3c) using simple control volume analysis. For each louver opening Λ , the velocity vectors were integrated over a three control surfaces ($x/c = 0$, $x/c = 10$, and $y/c = 7.5$ in the coordinate system of Figure V.2), and the flow rate into the

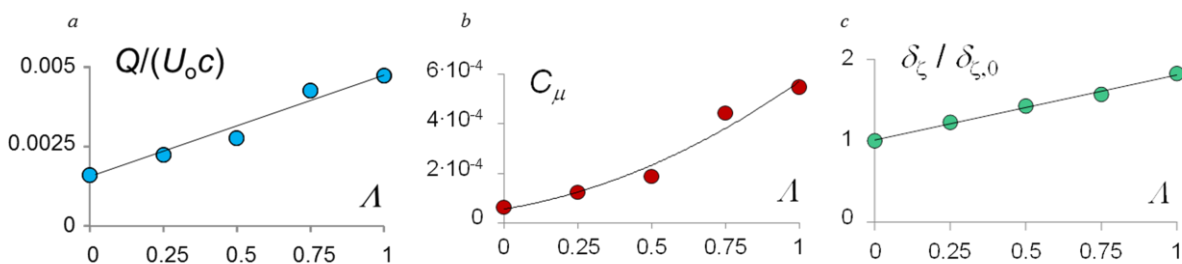


Figure V.3. Variation with fractional louver opening of: a) volume flow rate, b) momentum coefficient, and c) cross stream thickness of the vorticity layer.

frame was determined. Figure V.3a shows that the (normalized) bleed flow rate varies approximately linearly with the louvers' fractional opening, indicating primary dependence on the regulation of the flow resistance by the louvers since the driving pressure difference is nominally constant. It is noted that, even though the louvers are closed at $\Lambda = 0$, the substantial suction peak near the leading edge induces some flow from the bleed ports, which can be better controlled by improving the seal around the edges of the louvers. The volume flow rates in Figure V.3a correspond to extremely low momentum coefficients as shown in Figure V.3b, on the order of 10^{-4} for all bleed levels, underscoring the control authority of the self-regulating bleed. The variation of the cross-stream width of the shear layer with louver actuation (normalized by the vorticity thickness at $\Lambda = 0$) is shown in Figure V.3c. These data indicate that the shear layer's vorticity thickness varies linearly with Λ , and nearly doubles between $\Lambda = 0$ and 1 at $x/c = 0.15$ downstream from the bleed outlets even though the data in Figure V.2 suggest that the cross stream spreading does not increase significantly for $\Lambda = 0.75$ and 1. These results indicate that the bleed can effectively regulate the aerodynamic shape of the airfoil and consequently its aerodynamic performance.

V.2. Time-Dependent Bleed Actuation

Even though the temporal response to bleed actuation is limited by the internal fluidic passages within the airfoil model (the response of the louvers is well below 10 ms), it is noted that transient actuation (e.g., step change in actuation) leads to remarkably fast response of the measured forces and moments (considering the mass of the model and mounting system). Figure V.4 shows time traces of the force responses measured by the load cells to step (top-hat) bleed actuation [$\Lambda = (0, 1, 0)$]. At actuation onset, C_L and C_D experience a momentary increase before a decrease to a lower, quasi-steady level. It is notable that C_M sees a transient nose-down pitch of significant magnitude soon after actuation before settling to a steady value. These transients are damped within about $10T_{conv}$. As actuation ceases and the louvers close, C_L , C_D , and C_M return to their original levels without experiencing significant transient variations. Note that some ringing occurs during termination, either due to flow oscillations within the airfoil's cavity

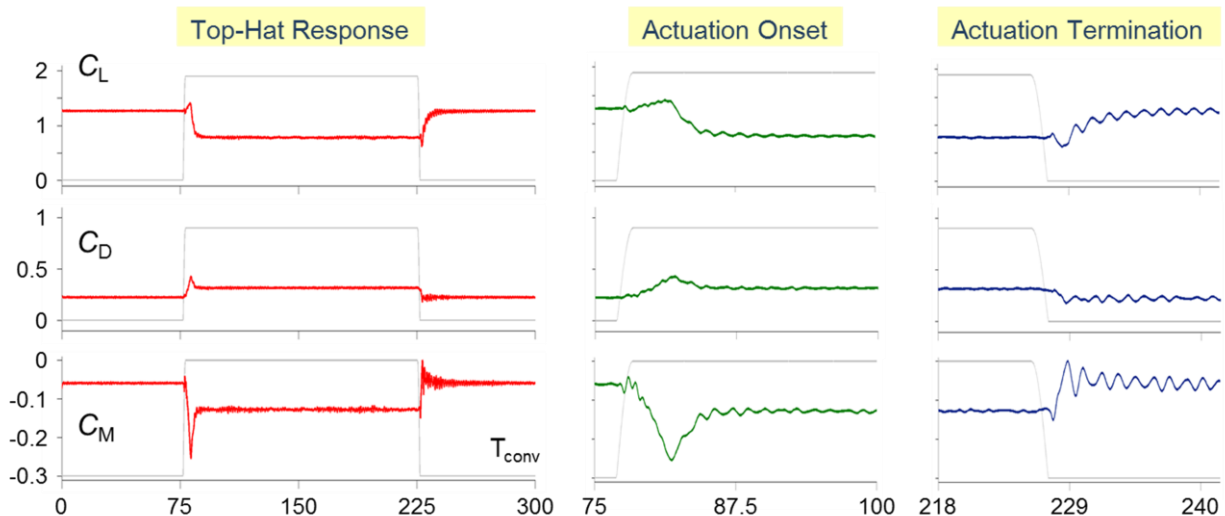


Figure V.4. Aerodynamic loading in response to a top-hat bleed actuation using leading-edge bleed ports. The actuation waveform is shown in gray, and magnified views of the actuation onset and termination are shown to the right. The oscillation frequency in the forces is nominally 55 Hz ($St_c = 0.73$).

or contact of the piezoelectric louvers with the airfoil surface. Figure V.4 also shows the force transitions on an expanded time scale. It is remarkable that the characteristic transitions in the lift, drag and pitching moment all occur on time scales of $10T_{conv}$.

Based on the aerodynamic response the transitory step in bleed, and the relevant characteristic time scales, it appears that these transients could be exploited by time-periodic bleed actuation to affect flow reattachment during stall. The louvers were operated at frequencies within the range $0.67 < St_{act} < 1.2$ (50-90 Hz in the present experiments) and the resulting pulsating bleed leads to significant post stall increases in lift.

The effects of the actuation on the static pressure distributions about the airfoil model are shown in Figure V.5 for the baseline airfoil and in the presence of bleed ($\Lambda = 0$ and 1) for several angles of attack (the pressure taps are placed on the surface of the structural grid that supports the bleed ports). These data show that at $\alpha = 14^\circ$ the flow over the baseline airfoil separates near $x/c = 0.45$, and the separation migrates upstream by $\alpha = 16^\circ$. At $\alpha = 18^\circ$, separation occurs near $x/c = 0.40$, but the suction peak increases significantly to nearly $C_p = -4.5$. This peak remains unchanged at $\alpha = 20^\circ$ as the separation moves to $x/c = 0.25$, and the airfoil becomes completely stalled at $\alpha = 22^\circ$. It is evident that the presence of some bleed (even at $\Lambda = 0$) leads to an upstream migration of the separation point and to a reduction in the pressure peak, suggesting that improved integration of the bleed may result in lower impact of the bleed ports on the aerodynamic performance at high angles of attack (this effect diminishes as the angle of attack is decreased). Increased bleed within the range $0 < \Lambda < 1$ eliminates the suction peak near the

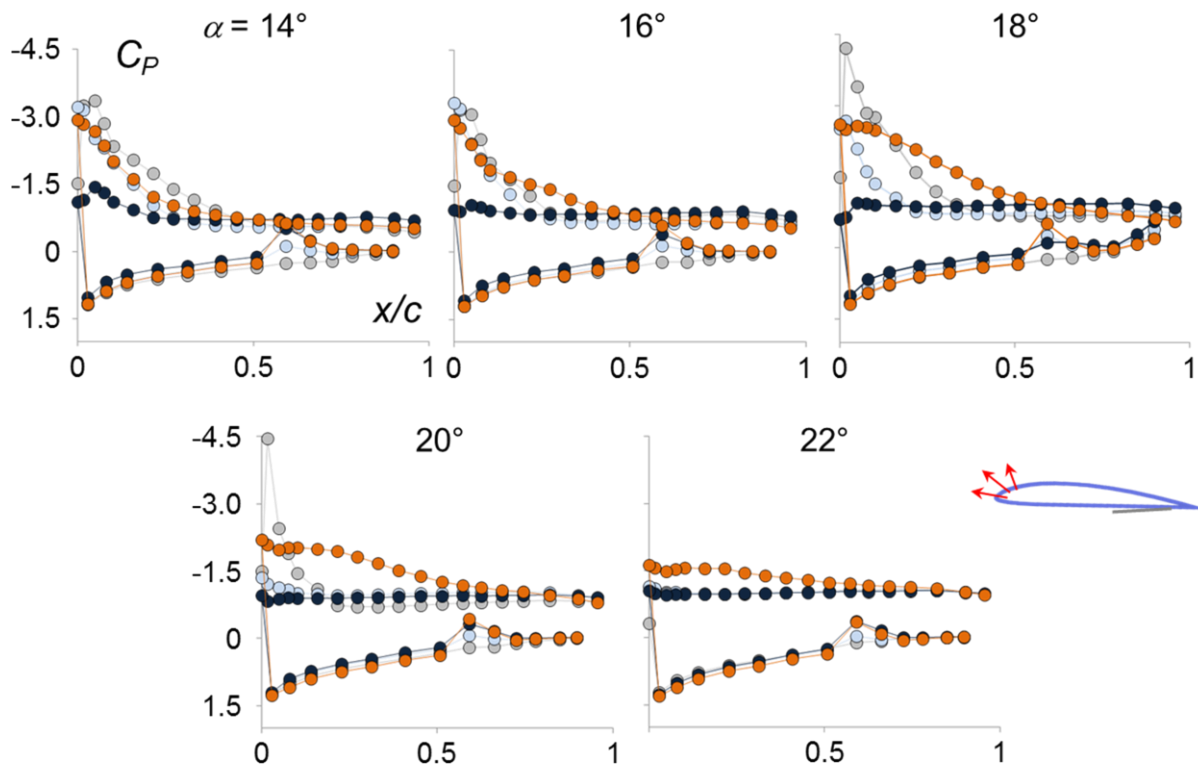


Figure V.5. Pressure distribution variations over the airfoil chord due to bleed through the leading edge over $\alpha = 14^\circ, 16^\circ, 18^\circ, 20^\circ,$ and 22° : baseline airfoil (\odot), $\Lambda = 0$ (\circ), $\Lambda = 1$ (\bullet), and high-frequency actuation (\bullet). Note the pressure-side peaks near $x/c = 0.6$ are due to the presence of the louvers.

leading edge as flow separation intensifies (cf. Figure V.2e) and results in a C_L decrement of nearly 0.6 (or nearly 39% compared to baseline). It is noteworthy that the bleed leads to a small reduction in the magnitude of the static pressure on the pressure side of the airfoil near the inlet to the bleed ports ($x/c \cong 0.6$).

Time-harmonic louver actuation alters the pressure distribution significantly. Although the suction peak is not fully restored for $\alpha = 16^\circ$ and 18° , the flow becomes nearly fully-attached along the entire top surface of the airfoil with significant increase in suction. When the airfoil experiences deep stall at $\alpha = 20^\circ$ and 22° , suction increases above baseline levels over the entire chord. The magnitude of the suction near the leading edge is clearly related to the apparent shape of the leading edge in the presence of bleed (cf. Figure V.7 below). Furthermore, the bleed also restores the pressure distribution on the pressure surface of the airfoil with the exception of the narrow domain that is influenced by the bleed inlet flow. The induced lift increment as a result of the actuation for the bleed configuration shown reaches a maximum at $\alpha = 18^\circ$ of $\Delta C_L = 0.23$.

The effect of time-harmonic bleed actuation on the range of attainable lift (for the static airfoil) is illustrated in Figure V.6a-c for three streamwise increments of the bleed outlet area on the suction surface ($0.056 < x/c < 0.07$, $0.03 < x/c < 0.07$, and $0.01 < x/c < 0.07$, respectively). The range within which the lift can be varied is marked for both quasi-steady (blue) and time-harmonic (orange) bleed actuation. To begin with, the lift range clearly increases with the streamwise extent of the bleed with the more significant differences between one and two bleed ports (Figures V.6a and b), which demonstrates that the separation can be intensified

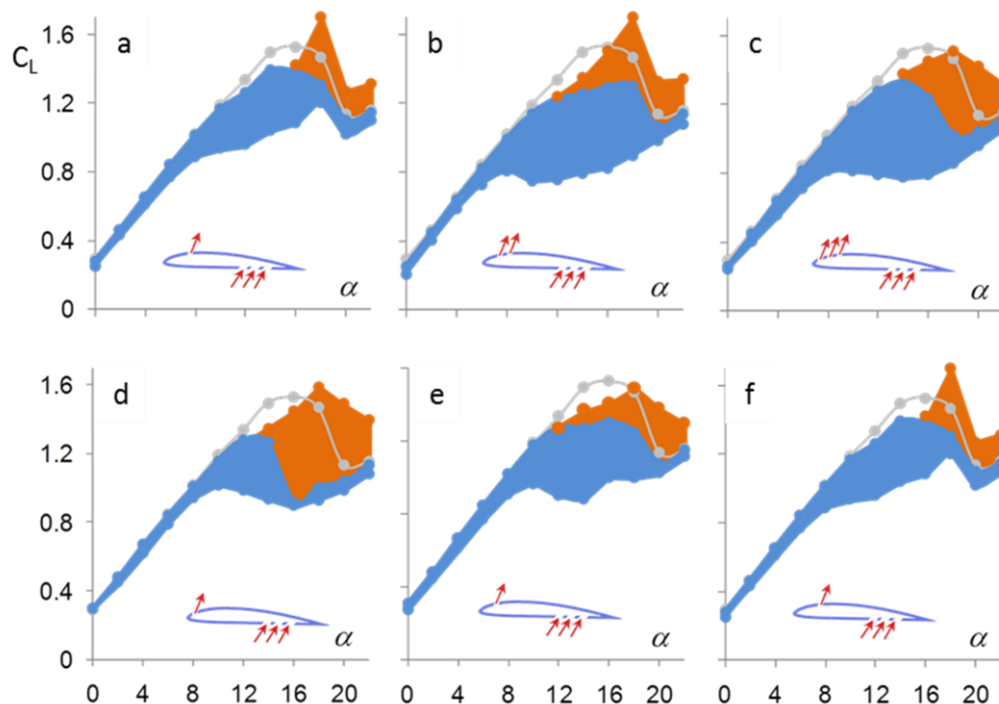


Figure V.6. Effective range of quasi-steady (blue) and time-harmonic (orange) bleed actuation. The lift variation of the baseline airfoil is shown in gray. In the top row, the streamwise extent of the bleed outlet ports on the suction surface is extended from $\Delta x/c = 0.014$ (a), to 0.04 (b) and to 0.06 (c). In the bottom row, the streamwise position of a single port is changed from $x/c = 0.014$ (a), to 0.035 (b), and to 0.062 (c).

significantly with increased bleed area. When time-harmonic actuation is applied, the bleed extends the range of the attainable lift beyond the levels of the baseline airfoil as marked in orange (with a small loss between 11° and 16°). It is interesting to note that the peak C_L (1.7 at $\alpha = 18^\circ$) can be attained by a single actuation port (Figure V.6a), but larger actuation area is more effective at higher angles of attack. Similarly, the effects of the streamwise position of the bleed port on the effectiveness range of bleed actuation are measured for a single spanwise bleed row with width $0.0125c$ centered about $x/c = 0.014$, 0.035 , and 0.062 as shown in Figures V.6d-e, respectively. Even though all three bleed rows are located upstream of separation when $\Lambda = 0$, the upstream port appears to provide the widest range of bleed control of the lift indicating that the magnitude of the pressure difference across the bleed path and perhaps the adverse pressure gradient on the suction surface influence the effectiveness.

These data demonstrate that bleed actuation can yield continuous adjustment of the lift within a broad domain of angles of attack ($8^\circ < \alpha < 22^\circ$). For example, for $\alpha = 18^\circ$, $0.9 < C_L < 1.7$ ($-0.57 < \Delta C_L < 0.23$ relative to the baseline) without the use of external control surfaces. These variations in C_L can be used for maneuvering (e.g., roll control), adjustment of spanwise lift distribution, or structural stabilization.

Finally, Figure V.7a-c shows three composite color raster plots of time-averaged spanwise vorticity concentrations over the entire airfoil at $\alpha = 18^\circ$ for $\Lambda = 0$, 1, and time-harmonic actuation, respectively, and the corresponding variations in aerodynamic forces. When $\Lambda = 0$ (Figure V.7a), the flow separates near $x/c = 0.25$, and the separated shear layer appears to be aligned with the free stream. This corresponds to the $C_L = 1.30$, near the upper bound of the (blue) domain for quasi-steady bleed for $C_L(\alpha)$, which shows a reduction compared to the baseline due to the presence of some bleed flow even when the louvers are closed (cf. Figure V.3) and the flow interaction with the open bleed outlets. However, when the louvers are completely open ($\Lambda = 1$, Figure V.7b), the interaction of the bleed flow with the separating shear layer leads to significant vectoring of its nominal centerline away from the airfoil (at an angle of 13° relative to the free stream) even though the bleed momentum coefficient is relatively low ($C_{\mu} = 5.47 \cdot 10^{-4}$). Of course, ultimately, the shear layer becomes aligned with the free stream downstream of the trailing edge of the airfoil. As noted in connection with Figure V.2e, the cross stream vorticity thickness doubles between $\Lambda = 0$ and 1. When $\Lambda = 1$, C_L reaches the lower bound of the domain, 0.90, while C_D variations are minimal, and nose-down C_M increases by 16%. When the louvers are actuated time-harmonically ($St_{act} = 1.2$, Figure V.7c), the flow becomes nominally attached and the actuation results in a thick vorticity layer above the surface of the airfoil with little evidence of recirculating flow, resulting in a $C_L = 1.7$. It appears that as a result of the actuation some of the shear layer vorticity is advected within the high-speed side of the shear layer ostensibly as a result of shedding that is phase-locked to the actuation. The flow attachment leads to stronger suction along the top surface of the airfoil as shown in Figure V.5. It appears that the interaction of the time-harmonic bleed actuation with the cross flow leads to the formation of a (time-average) domain of trapped vorticity downstream of the leading edge that enables the outer flow to overcome the adverse pressure gradient, and with it separation, resulting in increased lift.

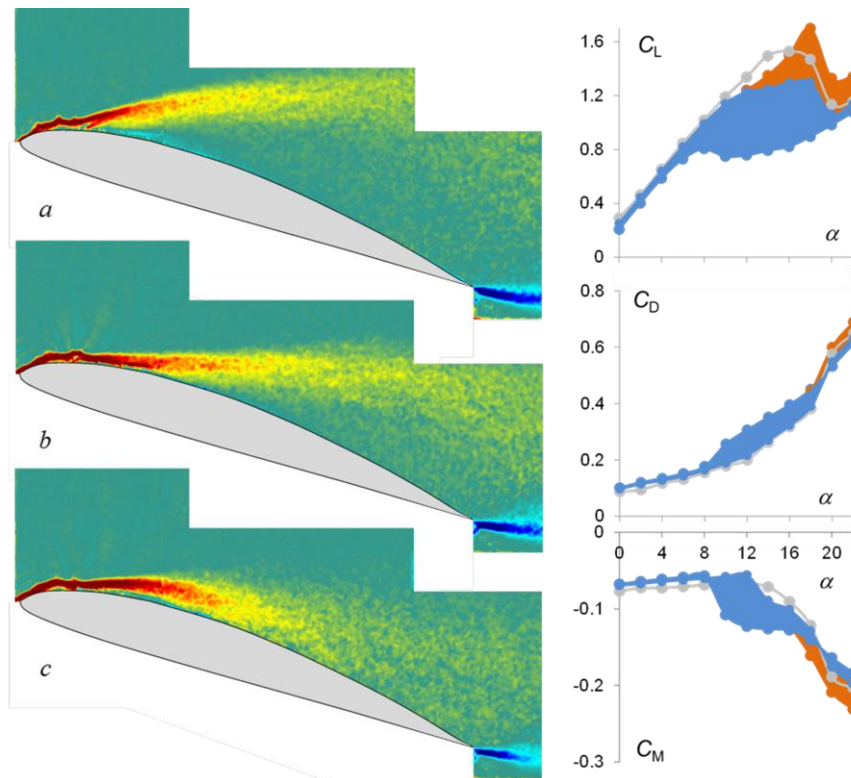


Figure V.7. Color raster plots of spanwise vorticity concentrations over the airfoil for $\Lambda = 0$ (a), 1 (b) and time-harmonic bleed actuation at $St_{act} = 1.2$ ($f_{act} = 90$ Hz) (c). Corresponding variations in C_L , C_D , and C_M due to bleed are shown at right.

VI. BLEED ACTUATION ON A PITCHING AIRFOIL

Dynamic stall significantly alters the flow about and the shedding of vorticity from an airfoil that is oscillating time-periodically in pitch with a significant increase in the stall angle due to convective flow time-lag effects and accelerated flow effects near the moving leading edge. The formation of the dynamic stall vortex and the accumulation of vorticity dominate the magnitude of an overshoot in $C_{L,max}$ by imposing a wall velocity in the boundary layer flow, thereby increasing momentum in the near-wall boundary layer and reducing the flow's tendency to separate (Ericsson and Reding, 1988). The transient region of clockwise dynamic stall vortex downstream of the leading edge builds during the airfoils upstroke as the reduced frequency $k = \omega c / 2U_\infty$ increases into the unsteady pitching regime. The accelerated flow effect causes this buildup by maintaining leading edge attachment while the cross-stream extent of the boundary layer downstream grows, trapping vorticity in a region between the leading edge and $x/c \approx 0.3$. When the dynamic stall angle is exceeded, the location of flow separation migrates upstream along the airfoil surface until the leading edge vortex is advected downstream, momentarily increasing local suction and augmenting C_L , while inducing a nose-up pitching moment C_M as it nears the trailing edge. When the vortex is advected into the wake, it leaves a separated domain over the airfoil behind it. As k and the pitch amplitude increase, the periodicity of the dynamic stall vortex's formation and shedding shifts out of phase with the oscillatory forcing, creating a corresponding phase lag in C_L and C_M as well as increasing the magnitudes of their variations.

During time-harmonic pitching at “low” (quasi-steady) reduced pitching frequencies

($k = \omega c / 2U_\infty \lesssim 0.08$), the lift of the baseline airfoil varies linearly with angle of attack through $\alpha \approx 10^\circ$ on both the up- and down-stroke of the pitch cycle, as shown in Figure VI.1a (gray). As the range of α increases to $5^\circ < \alpha < 15^\circ$, the flow begins to stall and some hysteresis is apparent. Stall is reached when $10^\circ <$

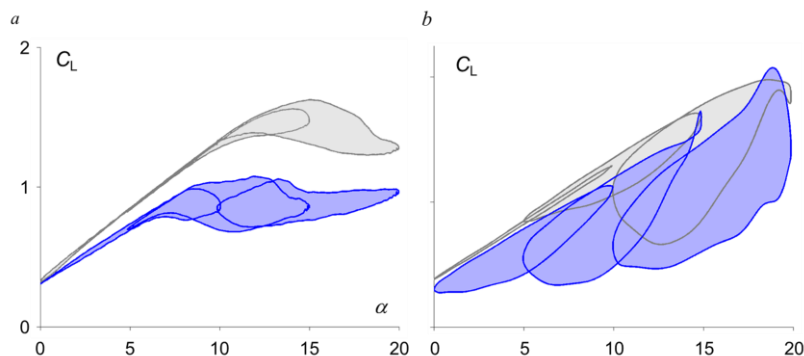


Figure VI.1. The range of influence of bleed actuation compared to the baseline airfoil during pitch at $k = 0.04$ (a) and 0.21 (b). Each plot is a composite of three ranges of α : $0^\circ < \alpha < 10^\circ$, $5^\circ < \alpha < 15^\circ$, and $10^\circ < \alpha < 20^\circ$. The shaded regions represent lift variations during pitch for the baseline (gray) and $\Lambda = 1$ (blue).

$\alpha < 20^\circ$ and the lift diminishes on the upstroke just beyond the static stall angle, and static levels of C_L are not recovered until pre-stall α is reached. However, as the reduced frequency increases beyond $k \approx 0.1$ (Figure VI.1b), the influence of unsteady aerodynamic effects on the time-periodic forces that are effected on the baseline airfoil increases as is evidenced for the cycle when $10^\circ < \alpha < 20^\circ$. The buildup of the dynamic stall vortex on the leading edge during the upstroke continues until $\alpha = 20^\circ$, leading to lift levels that exceed 40% of the maximum static value. As downstroke commences and the dynamic stall vortex is shed, the airfoil enters deep stall, reaching $C_{L,\min} = 0.6$ at $\alpha = 12^\circ$, equivalent to the static lift at $\alpha = 4^\circ$. Suction is restored on the upper surface as the airfoil continues the downstroke through the stable regime, and the cycle repeats.

Bleed has a profound effect on the evolution of the flow during the pitch cycle. Figure VI.1 shows the effect of continuous bleed at $\Lambda = 1$ both at quasi-steady and unsteady oscillation frequencies ($k = 0.04$ and 0.21). For low k (Figure VI.1a) the bleed lowers the range of attainable C_L similar to what was shown for the static airfoil (cf., Figure V.I). The data in Figure VI.1a also show that bleed can enable holding C_L (at a lower level relative to the baseline) nearly invariant over some range of α . At high reduced frequencies (Figure VI.1b), the flow variations induced by bleed actuation extend to $\alpha = 0^\circ$ for $0^\circ < \alpha < 10^\circ$ indicating that the bleed has the capability to significantly alter the dynamics of vorticity production and advection. For the higher ranges of α , the bleed can disrupt the separating shear layer and interact with the dynamic stall vortex to alter (and reduce) C_L and extend the hysteresis domain, widening the range of attainable lift force that is experienced by the airfoil.

The present investigation has also shown the ability of bleed actuation to affect the formation and evolution of the dynamic stall vortex, which can have a profound effect on the pitch stability of the cycle. The hysteresis associated with dynamic stall vortex is manifested in the $C_M(\alpha)$ curve by a sharp nose-down pitching moment when the vortex is shed. Directionality of the loop indicates whether the C_M acts to dampen the forced pitching motion or to reinforce the airfoil’s motion away from equilibrium, i.e. negatively damp the airfoil into an unstable mode such as flutter. Negative damping is observed when the area within a $C_M(\alpha)$ curve is enclosed in a clockwise direction, and stable motion occurs if the enclosure runs counterclockwise. Previous

work (e.g. Carta, 1967, Carta and Carlson, 1973) quantifies the extent of these enclosures by defining the two-dimensional aerodynamic damping coefficient, $E_\alpha = -\frac{\int C_M d\alpha}{\pi \bar{\alpha}^2}$, an integrated measure of the pitch stability with positive values indicating suppressive damping. Using this metric, it is found that bleed actuation increases the stability of the pitch motion and minimizes negative damping from quasi-steady and into unsteady pitching frequencies with relatively low penalty in cycle-averaged lift.

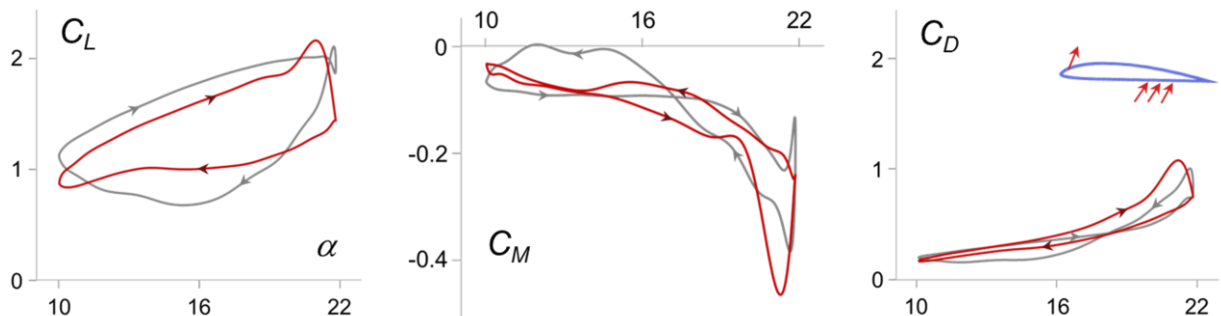


Figure VI.2. Cycle variations of C_L , C_M , and C_D at $k = 0.17$ for the baseline (gray) and in the presence of bleed burst ($f_{act} = 90\text{Hz}$, red) actuated between 20° (upstroke) and 10° (downstroke).

These effects are investigated when the actuation is applied at $k = 0.17$ in “bursts” at $f_{act} = 90\text{Hz}$ ($St_c = 1.2$) between $\alpha = 20^\circ$ (upstroke, $t/T_{cycle} = 0.14$) and 10° (downstroke, $t/T_{cycle} = 0.72$). Figure VI.2 compares distributions of C_L , C_M , and C_D during a pitch cycle of the airfoil for the baseline and in the presence of transitory actuation. As shown in Figure VI.2a, using this bleed configuration, the lift hysteresis during the downstroke is reduced while the penalty in cycle-averaged lift is about 8%. However, perhaps more important is the response of the pitching moment during the cycle. The baseline pitching moment exhibits clear crossover which indicates positive stability (CCW) between $10^\circ < \alpha < 17^\circ$ and negative stability (CW) between $17^\circ < \alpha < 22^\circ$. However, in the presence of bleed, the unstable segment of the cycle is fully eliminated during bleed actuation, where the pitch curve is entirely CCW and the entire cycle is stable. This is reflected in the differences in damping coefficients, $E_{\alpha, \text{baseline}} = 1.74\text{e-}4$ and $E_{\alpha, \text{bleed}} = 7.09\text{e-}4$. It is also noted that the drag increments during actuation are relatively small.

Deficits in time-averaged C_L using continuous high-frequency actuation ($f_{act} = 90\text{Hz}$) relative to the baseline over a pitch amplitude ranging from pre-stall to deep stall angles (i.e. through both static and dynamic stall angles) are shown in Figure VI.3 for a number of reduced frequencies. In the quasi-steady pitching regime, high-frequency actuation can maintain C_L to within 4–6% of baseline levels, while in the full unsteady regime it is effective to within 8–9%. In addition it is observed that lift augmentation relative to statically-actuated bleed using periodic transitory bursts of high-frequency actuation is comparable to that of continuous actuation. Applying actuation bursts at $f_{act} = 95\text{Hz}$ during half of the up- and downstrokes ($T_{act}/T_{conv} = 9.25$ and $T_{cycle}/T_{conv} = 18.75$) during pitch at

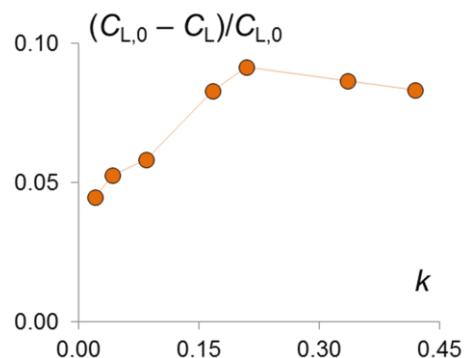


Figure VI.3. Variation with reduced frequency of percent decrease in cycle-averaged C_L relative to the baseline due to continuous, high-frequency actuation, $10^\circ < \alpha < 22^\circ$.

$k = 0.17$ reattaches the flow throughout the cycle, thereby limiting hysteresis during the downstroke and increasing lift compared to $\Lambda = 1$ by up to 40%. It is notable that C_L levels are augmented due to the dynamic bleed on the downstroke even after actuation ceases (Figure VI.2), which indicates that flow reattaches and remains so through the rest of the pitch cycle.

The increased pitch cycle stability using bleed actuation is evident over a range of reduced frequencies, as shown in Figure VI.4. Within the quasi-steady regime, the baseline airfoil begins to experience negative damping at $k \approx 0.2$, which intensifies in magnitude as k increases to fully unsteady. Below $k = 0.2$, bleed provides up to an order of magnitude more stability than what is achieved with the baseline airfoil. These data indicate that negative damping is postponed until $k = 0.26$. In the unsteady regime, high-frequency actuation yields a 58% increase damping compared to the baseline. It is remarkable that $\Lambda = 1$ yields higher stability compared to both the baseline and high-frequency bleed, but the penalty in lift is significant, and the damping becomes negative at high k .

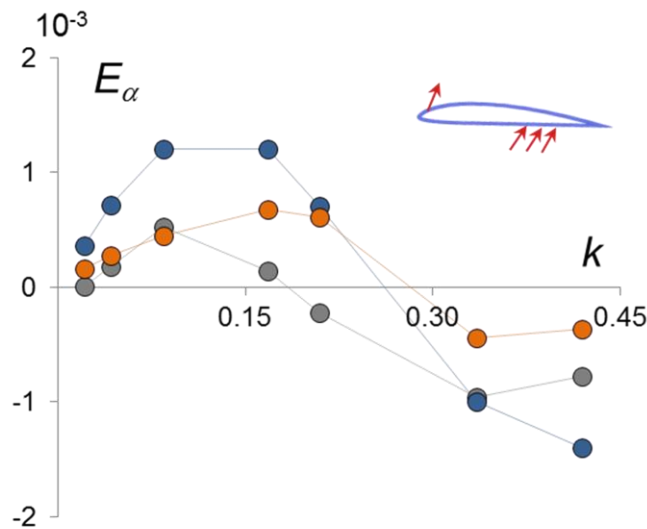


Figure VI.4. Variation of the aerodynamic damping coefficient with reduced frequency for baseline (\bullet), $\Lambda = 1$ (\bullet), and continuous high-frequency bleed ($f_{act} = 90\text{Hz}$, \bullet), pitching between $10^\circ < \alpha < 22^\circ$.

VII. CONCLUSIONS

A novel, scalable approach to aero-effected flight control of lifting surfaces using distributed active bleed is investigated experimentally and theoretically. Aerodynamic control is achieved by large-area surface bleed of air that is driven by the pressure differences in flight and is regulated by low-power surface-integrated louver actuators. The joint numerical-experimental investigation focuses on the flow mechanisms of the interaction between the bleed and the cross flow and aerodynamic effects of unsteady bleed on a 2-D wing model. Particular emphasis is placed on the generation and regulation of vorticity concentrations that alter the wing's apparent aerodynamic shape and thereby its aerodynamic performance over a range of (static) angles of attack, and under time-periodic pitch oscillations.

Wind tunnel investigations of the mechanisms of the time-dependent interactions between the bleed and cross flows utilize a 2-D Clark-Y model integrated with addressable arrays of piezoelectric louvers that are controlled from the laboratory computer through DC amplifiers for regulating leading and trailing edge bleed. Bleed is effected on the suction surface near the leading ($0.03 < x/c < 0.07$) or trailing ($0.76 < x/c < 0.85$) edges using controlled inlet ports on the pressure surface ($0.60 < x/c < 0.83$). The model is mounted on a programmable pitch system that enables arbitrary pitch variations at reduced frequencies up to $k = 0.42$ over a broad range of angles of attack, and the resulting time-dependent forces (C_L , C_D) and moment (C_M) are measured using integrated load cells.

The evolution of the flow in the presence of steady and unsteady bleed near the trailing edge of a static airfoil is investigated in closely-coupled experiments and numerical simulations using Navier-Stokes solvers that were specifically selected and modified to handle the complex geometries of airfoils with bleed. It is shown that bleed actuation near the trailing edge of the airfoil at low angles of attack modifies its aerodynamic characteristics when the baseline flow is fully attached. In particular, the pitching moment increment relative to the baseline and to the midpoint of louver opening (fractional opening $\Lambda = 0.5$) varies linearly with Λ within a range of about $\pm 12\%$ (positive change corresponds to nose up), and is nominally independent of α within the range $4^\circ < \alpha < 12^\circ$. The corresponding lift increment (relative to the baseline) decreases linearly with increasing Λ (about $\pm 6\%$ for $\alpha = 4^\circ$) indicating its utility for varying spanwise lift distributions or roll trim, but the effectiveness of the magnitude of the lift increments decreases somewhat with increasing α , ostensibly owing to the increase in the thickness of the boundary layer on the suction surface. It is noteworthy that these changes in C_M and C_L are accompanied by small changes in drag (up to $\pm 1.6\%$).

Detailed analysis of the computational and experimental trailing-edge bleed data shows that the induced changes in moment and lift coefficients vary as $\Delta C_M \approx -1/7 \Delta C_L$ for all bleed levels at all low to moderate α . Qualitative examination of the measured pressure distributions in the absence and presence of bleed show that trailing-edge bleed produces three primary aerodynamic effects. First, a local suction peak occurs on the pressure side of the airfoil in the vicinity of the inlet bleed slots. Second, at and downstream of the exit slots on the suction side, a local increase in (positive) pressure occurs corresponding to thickening of the boundary layer due to bleed. These two effects are termed *local* and produce negative lift due to bleed and positive (nose-up) moment because the center-of-pressure is located rearward of quarter chord $c/4$. Third, changes in pressure distribution near the leading edge also occur, a signature of a *global* effect that also produces negative lift. Subsequent analysis of the experimental pressure distributions determined that the local effects are responsible for two sevenths of the lift change and the corresponding center of pressure is at $3c/4$. In addition, the global effect is due to a change in airfoil circulation required to maintain the Kutta condition at the trailing edge in the presence of bleed. This latter change in circulation also corresponds to loss of lift due to bleed and accounts for five sevenths of the total change in lift coefficient with a center of pressure at $c/4$, in accordance with classical theory.

A vortex-based reduced order model is developed for trailing-edge bleed in close collaboration with the experimental effort. The model predicts unsteady airfoil lift and moment for an arbitrarily pitching and plunging airfoil with unsteady bleed by modeling the dynamics of discrete wake vortices and their circulations, as well as the dynamic specification of global and local vorticity distributions on the airfoil as a result of bleed. The latter specification was made possible by the analysis of measured distributions of static pressure in the absence and presence of bleed.

The effects of controlled bleed were also investigated at moderate and high angles of attack. Bleed actuation near the leading edge is effective between 8° and 20° and is manifested by a significant decrements in C_L (up to $\Delta C_L = 0.7$ at $\alpha = 16^\circ$) with relatively small penalty in drag (up to 0.1) and a stronger negative pitching moment. It is noteworthy that these changes are effected with low bleed momentum coefficient of up to $5.5 \cdot 10^{-4}$ (estimated from PIV measurements). Measurements of the interaction between the cross flow and the bleed near the surface using high-resolution PIV show that the bleed results in controlled degrees of flow

separation and lifting of the separated shear layer from the surface. It is shown that the angle of the separating shear layer relative to the free stream increases with the magnitude of the louver opening (even though the pressure difference decreases). The effective operating range of bleed actuation can be significantly extended by using time-harmonic actuation of the louvers ($0.6 < St_{\text{act}} < 1.2$) to enable lift increase at post-stall angles of attack beyond the level of the baseline airfoil. The actuation can be easily implemented with a time-invariant offset to enable combinations of steady and time-harmonic bleed. *The present investigation demonstrated that bleed actuation can yield continuous adjustment of the lift within a broad domain of angles of attack ($8^\circ < \alpha < 22^\circ$). For example, for $\alpha = 18^\circ$, $0.9 < C_L < 1.7$ ($-0.57 < \Delta C_L < 0.23$ relative to the baseline) without the use of external control surfaces. These variations in C_L can be used for maneuvering (e.g., roll control), adjustment of spanwise lift distribution, direct lift control (DLC) during landing, and for stabilization of flexible airframes (e.g., high-altitude UAVs).*

Finally, the effects of bleed actuation are also investigated on a pitching airfoil over a wide range of angles of attack. Bleed has a profound effect on the evolution of the flow during the pitch cycle. For quasi-steady (low k) oscillations the bleed lowers the range of attainable C_L similar to the effects on the static airfoil. The present measurements show that bleed can enable nearly invariant C_L (at a lower level relative to the baseline) over some range of α which may have implications for gust alleviation. At high reduced frequencies (unsteady regime, $k > 0.1$), bleed actuation has the capability to significantly alter the dynamics of vorticity production and advection even at low angles of attack when the flow is fully attached. For the higher ranges of α , the bleed can disrupt the separating shear layer and interact with the dynamic stall vortex to alter (and reduce) C_L and extend the hysteresis domain, widening the range of attainable lift force that is experienced by the airfoil. The present investigation also shows the ability of bleed actuation to affect the formation and evolution of the dynamic stall vortex and increase the stability of the pitch motion by minimizing negative damping (the aerodynamic damping coefficient is up to two times larger than in the baseline), with relatively low penalty in cycle-averaged lift, while reducing lift hysteresis.

REFERENCES

- Angot, P., Bruneau, C. H., and Fabrie, P., “A penalization method to take into account obstacles in incompressible viscous flows,” *Numerische Mathematik*, 81:497–520, 1999.
- Arquis, E., and Caltagirone, J.-P., “Sur les conditions hydrodynamique au voisinage d’une interface milieu fluide-milieu poreux; application à la convection naturelle,” *Comptes Rendus de l’Academie des Sciences Paris*, 299 (Série II):1–4, 1984.
- Bauer, S. X. S., and Hensch, M. J., “Alleviation of Side Force on Tangent–Ogive Forebodies Using Passive Porosity,” *J. Aircraft*, **31**, 354–361, 1993.
- Carpenter, P. and Porter, L., “Effects of Passive Porous Walls on Boundary-Layer Instability,” *AIAA J*, **39**, 597-604, 2001.
- Carta, F. O., “An Analysis of the Stall Flutter Instability of Helicopter Rotor Blades,” *Journal of the American Helicopter Society*, **12**, 1-18, 1967.
- Carta, F. O., and Carlson, R. G., “Determination of Airfoil and Rotor Blade Dynamic Stall Response,” *Journal of the American Helicopter Society*, **18**, 31-39, 1973.
- Chang, W., Giraldo, F., and Perot, B., “Analysis of an exact fractional step method,” *Journal of Computational Physics*, 180: 183–199, 2002.
- Coloni, T., and Taira, K., “A fast immersed boundary method using a nullspace approach and multi-domain far-field boundary conditions,” *Computer Methods in Applied Mechanics and Engineering*, 197:2131–2146, 2007.
- Corke, T. C., and Post, M. L., “Overview of Plasma Flow Control: Concepts, Optimization, and Applications,” AIAA Paper 2005-563.
- Ericsson, L. E., and Reding, J. P., “Fluid Mechanics of Dynamic Stall Part I. Unsteady Flow Concepts,” *Journal of Fluids and Structures*, 2:1-33, 1988.
- Fan, X. and Brown, G., “Experiments on the Electromagnetic Control of Turbulence,” AIAA-Paper 1997-2123, 1997.
- Frink, N. T., Bonhaus, D. L., Vatsa, V. N., Bauer, S. X. S., and Tinetti, A. F., “Boundary Condition for Simulation of Flow Over Porous Surfaces,” *J. Aircraft*, **40**, 692-698, 2003.
- Gazzola, M., Chatelain, P., van Rees, W.M., and Koumoutsakos, P., “Simulations of single and multiple swimmers with non-divergence free deforming geometries,” *Journal of Computational Physics*, 230: 7093–7114, 2011.
- Glezer, A. and Amitay, M., “Synthetic Jets,” *Ann Rev Fluid Mech*, 24, 2002.
- Han, Y., and Leishman, J., “Investigation of Helicopter Rotor-Blade-Tip-Vortex Alleviation Using a Slotted Tip,” *AIAA J*, **42**, 524-535, 2004.
- Ho, S., Nassef, H., Pornsinsirak, N., Tai, Y.-C., and Ho, C.-M., “Unsteady Aerodynamics and Flow Control for Flapping Wing Flyers,” *Prog Aero Sci*, **39**, 635–681, 2003.
- Hunter, C.A., Viken, S.A., Wood, R.M., and Bauer, S.X.S., “Advanced Aerodynamic Design of Passive Porosity Control Effectors,” AIAA paper 2001 -0249, 2001.
- Lachmann, G., “Results of Experiments with Slotted Wings,” NACA TM 282, 1924.

- Liepmann, H. W., and Nosenchuck, D. M., “Active control of Laminar-Turbulent Transition,” *J. Fluid Mech*, 118, 201-204, 1982.
- Liu, C., Tsao, T., Tai, Y., and Ho, C., “Surface Micromachined Magnetic Actuators,” *Proceedings IEEE Micro Electro Mechanical Systems*, 57-62, 1994.
- Lopera, J., Ng, T. T., and Patel, M. P., “Experimental Investigations of Reconfigurable Porosity for Aerodynamic Control,” AIAA Paper 2004-2695, 2004.
- Mittal, R., and Iaccarino, G., “Immersed boundary methods,” *Annual Review of Fluid Mechanics*, 37:239–261, 2005.
- Patel, M. P., DiCocco, J. M., Prince, T. S., and Ng, T. T., “Flow Control Using Reconfigurable Porosity,” AIAA paper 2003-3665.
- Perot, J., “An analysis of the fractional step method,” *Journal of Computational Physics*, 108:51–58, 1993.
- Peskin, C., “The immersed boundary method,” *Acta Numerica*, 11:479–517, 2002.
- Press, W. H., Flannery, B. P., and Teukolsky, S. A., “Numerical Recipes in C,” *Cambridge University Press*, 1992.
- Rossinelli, D., Bergdorf, M., Cottet, G.-H., and Koumoutsakos, P., “GPU accelerated simulations of bluff body flows using vortex particle methods,” *Journal of Computational Physics*, 229:3316–3333, 2010.
- Savu, G., and Trifu, O., “Porous Airfoils in Transonic Flow,” *AIAA J*, **22**, 989–991, 1984.
- Taira, K., and Colonius, T., “The immersed boundary method: A projection approach,” *Journal of Computational Physics*, 225:2118–2137, 2007.
- Tanner, M., “Reduction of Base Drag,” *Prog Aero Sci*, **16**, 369-384, 1975.
- Tchieu, A. A., and Leonard, A., “A discrete-vortex model for the arbitrary motion of a thin airfoil with fluidic control,” *Journal of Fluids and Structures*, 27:680-693, 2011.
- Tinetti, A. F., Kelly, J. J., Bauer, S. X. S., and Thomas, R. H., “On the Use of Surface Porosity to Reduce Unsteady Lift,” AIAA Paper 2001-2921, 2001.
- Weick, F. E., and Shortal, J. A., “The Effect of Multiple Fixed Slots and a Trailing Edge Flap on the Lift and Drag of a Clark-Y Airfoil,” NACA Report No. 427, 1932.